Snap Transitions in Adhesion

Richard M. Springman and John L. Bassani[1]
Mechanical Engineering Department, University of Pennsylvania, 220 S. 33rd Street, Philadelphia, PA 19104, USA

Abstract

Equilibrium adhesion states are analyzed for nonlinear spherical caps adhered to a rigid substrate under the influence of adhesive tractions that depend on the local separation between the shell and substrate. Transitions between bistable snapped-in and snapped-out configurations are predicted as a function of four nondimensional parameters representing the adhesive energy, the undeformed shell curvature, the range of the adhesive interactions, and the magnitude of an externally applied load. Non-uniform energy and traction fields associated with free-edge boundary conditions are calculated to better understand localized phenomena such as the diffusion of impurities into a bonded interface and the diffusion of receptors in the cell membrane. The linear Griffith approximations commonly used in the literature are shown to be limited to shells with a small height to thickness ratio and short-range adhesive interactions. External loading is shown to alter the adhered configurations and the spatial distributions of both adhesive and elastic energies. An important implication of the latter analysis is the theoretical prediction of the pull-off force, which is shown to depend not only on the interface properties, but also on the geometric and material parameters of the shell and on both the magnitude and type of external loading.

Keywords: Adhesion; Shell mechanics; Wafer bonding; Cell adhesion; Pull-off

1. Introduction

The adhesion of thin shell structures either to other shells or to substrates plays an important role in many micro- and nano-mechanical systems in engineering and biology. Geometric nonlinearities associated with finite shell deformations and the highly nonlinear nature of the adhesive interactions complicates our understanding of these complex and important systems. In this paper bistable (static) equilibrium states are studied to develop a more fundamental understanding of nonuniform adhesion. Specifically, this paper investigates the adhesion of spherical caps interacting nonlinearly with a rigid substrate through an adhesion law that is derived from Lennard-Jones interactions. Bulk adhesion parameters are described that represent the strength and range of the adhesive interactions. These adhesion parameters are taken to describe the cumulative interactions between the surfaces, including electrostatic forces, Van der Waals forces, steric repulsion, and the specific forces of fixed surface groups. Theoretical (Muller, Deryagin and Toporov, 1983; Israelachvilli, 1985; Maugis, 2000) and experimental (Israelachvili and Tabor, 1972; Klein, 1982; Leckband et al., 1992; Leckband et al., 1994; Wong et al., 1997; Leckband and Israelachvili, 2001) support for the adopted adhesion law is available in the literature.

[1] Corresponding author.
E-mail address: bassani@seas.upenn.edu (John L. Bassani)

Nonlinear shallow shell theory is used to study the elastic deformations of the shell structures (Reissner, 1950; Budiansky, 1959; Sanders, 1963; Niordson, 1985). An important implication of the free-edge boundary conditions considered in this analysis is the inadmissibility of perfectly bonded configurations, which also are excluded by compatibility in the case of closed vessels. The coupling between shell bending and stretching, as captured with nonlinear shallow shell theory, is shown to play a particularly important role in adhesion, which typically involves the deformation of curved shell surfaces into nearly planar configurations. Such configurations can not be achieved with a length preserving (isometric) mapping when the undeformed shell surface has a nonzero Gaussian curvature (Stoker, 1969). Nonlinear effects associated with this coupling are important once the magnitude of the normal displacement approaches half the shell thickness (Reissner, 1950), which can occur for adhesion if the reference shell height is greater than or equal to the shell thickness.

The vast majority of prior work on the adhesion of elastic bodies assumes the adhesive energy of the system is directly proportional to the area of an ideally bonded region (Seifert, 1991; Mastragelo and Hsu, 1993; Sackmann and Bruinsma, 2002; Turner and Spearing, 2002; Freund and Yuan Lin, 2004; Graf et al., 2006). Since this is analogous to the approach taken by Griffith in studies of brittle fracture (Griffith, 1921), this estimate of the adhesive energy is referred to as a Griffith approximation. Kinematical conditions on the displacement field required to ensure compatibility between the bonded and unbonded surface regions result in a separation profile with discontinuous derivatives of second order and higher at the adhesion front, which implies a jump in bending-moment that has not been justified physically. Several steps have been taken to treat the adhesive energy in a more general way. For example, Seifert (1991) studied the adhesion of inextensible, two dimensional (cylindrical) membranes to a rigid half-space by minimizing the sum of the Helfrich bending energy (Helfrich, 1973) and the adhesive energy. In that work the adhesive energy is treated both by Griffith approximations and by considering a finite range adhesive potential that has a dependence on the local separation between the membrane and half-space. In the limit of short-range interactions and moderate to large adhesive energy, the computed vesicle shapes of both formulations agree well. More recently, Komura et al. (2005) modeled a spherical shell as a network of tethered springs and determined adhered states by minimizing a discrete energy functional that includes stretching of the springs, an approximate description of bending resistance, and an adhesive potential that depends on the local separation between the nodal points and a rigid half-space. In addition, they use that analysis to infer continuum properties by comparison with *linear* measures of strain. Unlike these prior works, the analysis in this paper accounts for nonlinear coupling between the bending and stretching deformations of a continuum shell and finite-range adhesion interactions.

Shell analysis is applicable to wafer bonding, the adhesion of metallic nanocaps (Love et al., 2002; Charnay et al., 2003; Chen et al., 2004), the adhesion of lipid vesicles with finite shear resistance (Evans and Skalak, 1980; Secomb, 1988; Boal, 2002), in micro-mechanical structures (Maboudian and Howe, 1997), and to approximately model the adhesion induced deformation of biological cells. In the latter case, it is important to note that the cell membranes of eukaryotic cells are stiffened by transmembrane proteins and are supported by a filamentous structure called the actin cortex (Boulbitch et al., 2000; Lang et al., 2000; Pesen and Hoh, 2005), while different structures support the membranes of prokaryotic cells (e.g. bacteria) (Boal, 2002). Therefore, in the context of living cells the shell structural and material properties should be associated with the effective behavior of the cell membrane and attached protein networks. Force generation associated with active structural reorganization (Dobereiner et al., 2004; Reinhart-King, Dembo

and Hammer, 2005) accompanies the adhesion of many living cells over long time periods, which may limit the applicability of this elastic analysis in studies of these cell types. However, the initial stages of adhesion that occur without structural reorganization are important in their own right. In particular, the traction forces exerted during initial contact are believed to trigger the assembly of focal adhesion complexes, which in turn initiate the mechanical signals required for actin polymerization and myosin driven contraction (Galbraith et al., 2002). Furthermore, the nonuniform distributions of adhesive energy and tractions presented in this paper are a general characteristic of adhesion whenever the interacting surfaces are not perfectly bonded over their entire domain.

Although the mechano-chemical coupling that occurs in the presence of mobile chemical species is not explicitly considered in this analysis, the presented results have some general implications for the coupled system. Most notably, the spatially nonuniform energy fields that are a feature of mechanical equilibrium also result in nonuniform equilibrium distributions of chemical species (Freund and Yuan Lin, 2004). Wafer bonding (Mirza and Ayon, 1999), the adhesion of drug delivery microcapsules (Chen et al., 2004), and the adhesion of biological cells are important examples of systems where this coupling is important. For example, in wafer adhesion the diffusion of impurities such as water into the interface results in bond degradation (Tsui et al., 2006). Alternatively, the diffusion of integrin molecules in the cell membrane plays a critical role in the formation of adhesive linkages, which in turn regulate downstream cell function (Guttenberg et al., 2000; Galbraith et al., 2002; Freund and Yuan Lin, 2004; Smith et al., 2006; Smith and Seifert, 2007).

Important findings of this work are: adhesive transitions between stable snapped-in and snapped-out configurations; nonuniform distributions of adhesive and elastic energies at equilibrium; and a strong dependence of the pull-off force on the type of external loading. Solutions are presented for a range of parameters that result in both bending and stretching dominated structural responses and in varying degrees of nonuniform spatial distributions. Furthermore, the results show that a linear Griffith analysis is only accurate in the limiting case of short-range interactions and small curvature shells, for which the total adhesive energy at equilibrium is roughly proportional to the area of an ideally bonded central region. Furthermore, the jump in moment that occurs at the edge of the ideally bonded region under Griffith (Turner and Spearing, 2002) is shown to be the result of a force couple formed by adhesive tractions.

2. Adhesion Model

Consider a shallow spherical cap adhering to a rigid half-space. The shell is loaded by adhesive tractions T and a uniform external load P_{ext}, both acting in the vertical direction. Axisymmetric deformations are considered with dependence only on the radial coordinate r. In the reference configuration the spherical cap has a thickness t, a curvature κ, and a vertical separation z_i that is given by:

$$z_i = \frac{1}{2}\kappa r^2 + z_o, \tag{1}$$

where z_o is an arbitrary constant (see Fig. 1). The curvature is related to the projected shell radius a and the shell height $H = z(a) - z(0)$ by $\kappa = 2H/a^2$. The tangent angle of the

undeformed shell is $dz_i/dr = \kappa r$ and the vertical offset between the middle and bottom shell surfaces is approximately $t/2$.

An adhesive material layer with continuum thermodynamic properties resides between the shell and substrate (Cahn, 1979; Guggenheim, 1993). The shell, adhesive layer, and substrate are imagined to constitute a closed thermodynamic system. The temperature and the concentration of adhesive (or impurity) species in the layer are considered uniform and constant. The shallow shell is capable of moderate rotations, but is restricted to small strains (projected area approximately constant). The elastic strain energy of the shell is denoted by u_e and the work of the externally applied load by w_{ext}, both defined per unit area of the middle shell surface (Budiansky, 1968). Furthermore, the tractions T associated with the adhesive layer are taken as conservative and, therefore, derivable from an adhesive potential u_a. For this system the total potential energy is postulated to take the form:

$$U_t = 2\pi \int_0^a \left[u_e + u_a - w_{ext} \right] r \, \mathrm{d}r \,. \tag{2}$$

2.1. The Adhesive Law

The adhesive interactions between two bodies, in general, depend on the atomic interactions between the bulk materials, the surface chemistry and charge, and the surrounding medium. Despite the complexity of the underlying physics, the effective behavior of the adhesive layer is generally characterized by moderate range attractive interactions and short-range repulsive interactions (Israelachvilli, 1985; Maugis, 2000). Examples include the interactions between mica surfaces (Israelachvili and Tabor, 1972), polymer layers in solvent (Klein, 1982; Taunton et al., 1988), and the interactions of receptor-ligand systems (Leckband et al., 1992; Leckband et al., 1994; Wong et al., 1997). These general observations are captured by adopting a simple and classical description of the adhesive potential that is derived from Lennard-Jones interactions.

The adhesive potential u_a and corresponding tractions T are taken in the form (see Fig. 2):

$$u_a(z) = -\frac{3\sqrt{3}\,(\sigma_m \delta_o)}{4}\left[\left(\frac{\delta_o}{z}\right)^2 - \frac{1}{4}\left(\frac{\delta_o}{z}\right)^8\right], \quad T(z) = \frac{3\sqrt{3}\;\sigma_m}{2}\left[\left(\frac{\delta_o}{z}\right)^3 - \left(\frac{\delta_o}{z}\right)^9\right], \tag{3}$$

where $\sigma_m = T(1.20\,\delta_o)$ is the maximum adhesive traction and the equilibrium (lowest energy) separation δ_o sets the range of the interactions, which become vanishingly small for separations larger than about $10\,\delta_o$. The work of adhesion corresponding to (3) is given in terms of σ_m and δ_o by:

$$W_{ad} = \int_{\delta_o}^{\infty} T(z)\,\mathrm{d}z = \frac{9\sqrt{3}}{16}(\sigma_m\,\delta_o)\,. \tag{4}$$

Theoretically, the adhesion law (3) corresponds to the interaction between two Lennard-Jones half-spaces and has been used to account for the adhesive interactions in other models (Muller et al., 1983; Maugis, 2000). Similar adhesion laws have been adopted elsewhere (Seifert, 1991; Mishin et al., 2002; Komura et al., 2005). The equilibrium separation δ_o should not be interpreted as the equilibrium length scale of an atomistic potential (Yu and Polycarpou, 2004), but should be regarded as a bulk adhesion parameter. Similarly, the work of adhesion

W_{ad} and the interface strength σ_m are also considered bulk parameters in this analysis, representing all physics that contribute to the effective behavior of the adhesive layer. However, in interpreting the results that follow, the work of adhesion can be viewed to depend on the uniform surface concentrations of adhesive or impurity species.

2.2 Governing Equations for Axisymmetric Deformations of a Spherical Cap

Shell deformation is modeled using Reissner's nonlinear shallow shell equations for thin shells of revolution undergoing axisymmetric deformations with small in-plane strains and moderate rotations (Reissner, 1950; Wan and Weinitschke, 1988). Linear elastic isotropic material behavior is assumed. In the shallow limit, the strain-displacement relations associated with these equations are equivalent to those given by Sanders for small strains and moderate rotations (Sanders, 1963) and to those of the Donnel-Mushtari-Vlasov (DMV) theory (Niordson, 1985). Equivalent forms of these equations are prevalent in the literature on shell buckling (Weinitschke, 1958; Budiansky, 1959). Thin shells are defined as having a ratio $t/R \ll 1$, where R is the radius of curvature and t is the thickness. According to Reissner, the shallowness requirement is given in terms of the shell height H and projected shell radius a by $H/a \lesssim 1/6$ (Reissner, 1958).

A natural choice of solution variables is the separation of the deformed shell z and the membrane stress function ψ, analogous to the Airy stress function in plane elasticity. The change in tangent angle (rotation) β is related to the separation by:

$$\beta = \frac{dz_i}{dr} - \frac{dz}{dr} = \kappa r - \frac{dz}{dr} \tag{5}$$

The nonlinear, coupled Euler-Lagrange equations of equilibrium associated with a stationary point in the potential energy functional (2) are given as:

$$\frac{Et^3}{12\left(1-\nu^2\right)}\left(r\frac{d^2\beta}{dr}+\frac{d\beta}{dr}-\frac{1}{r}\beta\right)+\left(\frac{dz}{dr}\right)\psi-\int_0^r T\left(z\right)r'\,dr'+\frac{P_{ext}}{2}r^2=0\ , \tag{6}$$

$$\frac{1}{Et}\left(r\frac{d^2\psi}{dr^2}+\frac{d\psi}{dr}-\frac{1}{r}\psi\right)-\left(\frac{dz_i}{dr}\right)\beta+\frac{1}{2}\beta^2=0\ , \tag{7}$$

where $T\left(z\right)$ is the adhesive law defined in (3). The nonlinear term in (6) accounts for the coupling between bending and stretching of the shell, whereas the nonlinear term in (7) accounts for finite rotations. An additional loading nonlinearity enters through the integral term in (6). Uniqueness can not be guaranteed due to finite geometry changes and nonlinearity associated with adhesive tractions derived from a nonconvex potential and, in fact, bistable and unstable solutions are found to exist. Therefore, a stable solution may correspond to a local minima (metastable) or global minimum (absolutely stable) of the potential energy.

2.3 Boundary Conditions

For unconstrained adhesion of a free-standing, open shell the moment, shear force, and radial membrane force must vanish at the shell boundary. These conditions are given, respectively, as:

$$M_r\big|_{r=a} = \frac{Et^3}{12\left(1-\nu^2\right)}\left[\frac{d\beta}{dr}+\frac{\nu}{r}\beta\right]_{r=a} = 0\,, \tag{8}$$

$$Q\big|_{r=a} = \frac{Et^3}{12\left(1-\nu^2\right)}\left[\frac{d^2\beta}{dr}+\frac{1}{r}\frac{d\beta}{dr}-\frac{1}{r^2}\beta\right]_{r=a} = 0\,, \tag{9}$$

$$\psi\big|_{r=a} = 0\ . \tag{10}$$

Additionally, symmetry requires that the shell slope and radial displacement vanish at the apex. Rigid body displacements of the shell are only constrained by the requirement of overall equilibrium. This fact is more evident if the shear force requirement written in (9) is replaced by the equivalent requirement of overall force equilibrium:

$$-2\pi\int_0^a T\left(z\right) r\,dr + \pi a^2 P_{ext} = 0\ . \tag{11}$$

There are two subtle, yet important implications of boundary conditions (8) - (11). First, the solution for perfect bonding $\left(z=\delta_o,\ \beta = dz_i/dr\right)$ is not admissible unless the undeformed shell geometry satisfies certain boundary conditions, which are found by substituting the flat solution into boundary conditions (8) and (9). For the spherical cap given by (1) the perfectly bonded solution is $z=\delta_o$, $\beta=\kappa r$, and $\psi = Et\kappa^2 r\left(r^2-a^2\right)\big/16$. The moment condition (8) is not satisfied by this solution and, therefore, either an applied moment $M_r\big|_{r=a} = -Et^3\kappa\big/12\left(1+\nu\right)$ or a flat geometry $\kappa=0$ is required for perfect adhesion. All equilibrium configurations for $\kappa\neq 0$ and $M_r\big|_{r=a}=0$ will involve nonuniform adhesion to the substrate. Second, the vertical equilibrium requirement (11) requires that the repulsive and attraction tractions on the shell surface balance the applied load. Since nonuniform adhesion is guaranteed from the boundary conditions whenever $\kappa\neq 0$, nonzero adhesive tractions must load the shell at equilibrium, even in the absence of applied load.

2.4. Nondimensional Variables

The nondimensional groups most useful for characterizing solutions are:

$$\tilde{W}_{ad} = \frac{W_{\text{ad}}}{Et^3\kappa^2},\quad \tilde{P}_{ext} = \frac{P_{ext}}{E\left(\kappa t\right)^2},\quad \lambda = \frac{\kappa a^2}{t},\quad \tilde{\delta}_o = \frac{\delta_o}{t}\ , \tag{12}$$

where the nondimensional work of adhesion $\tilde{W}_{ad}$ measures the relative importance of adhesive and elastic energies, the nondimensional range $\tilde{\delta}_o$ sets the range of the adhesive interactions relative to the shell geometry, and the dimensionless curvature λ determines the relative importance of shell bending and stretching. The nondimensional external load $\tilde{P}_{ext}$ is directly proportional to the approximate buckling pressure of a uniformly loaded shallow spherical cap (Hutchinson, 1967), which for a Poisson's ratio of $\nu=0.3$ is $P_{cr}=1.21E\left(\kappa t\right)^2$. The ratio $H/\delta_o = \lambda/2\tilde{\delta}_o$ is found to determine the spatial distribution of adhesive energy.

The loading variables are $\tilde{W}_{ad}$ and $\tilde{P}_{ext}$. In this regard, a scenario is imagined where the elastic and geometric properties of the shell are fixed and either W_{ad} or P_{ext} is varied. Load induced shell flattening is conveniently characterized by the *flatness parameter* Φ, defined as:

$$\Phi = \int_0^a \left| \frac{z(r) - z(0)}{z_i(r) - z_i(0)} \right| r\, dr \,. \tag{13}$$

When Φ=1 the shell is undeformed and when Φ=0 the shell is perfectly flat.

Values of the nondimensional parameters (12) are estimated for wafer bonding, the adhesion of nanocaps, cell adhesion, and the adhesion of lipid vesicles in Table 1. The estimates are based on geometric and material parameters taken from the literature. Wafer bonding is generally characterized by small curvatures, short-range interactions, and a small work of adhesion. The dimensions and material properties considered for nanocaps result in moderate range interactions, moderate curvatures, and a small work of adhesion, although the caps can generally be manufactured to a variety of specifications. For the cell, the Young's modulus and thickness are identified with measured properties of the actin cortex (Lang et al., 2000; Pesen and Hoh, 2005), the reference curvature is typical of a spherical cell, and the equilibrium separation is estimated from experiment (Izzard and Lochner, 1976). For these estimates, cell adhesion generally involves moderate range adhesive interactions, large curvatures, and a large work of adhesion. Due to the extremely small thickness of lipid membranes, both the nondimensional curvature and work of adhesion are very large.

2.5. Numerical Analysis

The governing equations (6) - (7) , the definition of the rotation (5), and the boundary conditions (8) - (10) are discretized using finite differences and a quadrature rule. Converged solutions to the discretized equations are obtained using a tangent predictor step and a Gauss-Newton corrector step (Allgower and Georg, 1997) treating either the nondimensional work of adhesion $\tilde{W}_{ad}$ or the external load $\tilde{P}_{ext}$ as a solution variable. This continuation algorithm allows calculation of both stable and unstable equilibrium solution curves as a function of the load parameters. Details of the discretization and solution procedures are given in the Appendix. Solutions are presented for values of the nondimensional curvature λ = 1, 6, 12, and 18, and the nondimensional range $\tilde{\delta}_o$ = 10, 1, 0.1, 0.01, and 0.001. For all solutions Poisson's ratio $\nu = 0.3$.

3. Equilibrium Solutions in the Absence of External Load

Equilibrium states for a spherical cap deformed only by adhesive tractions ($\tilde{P}_{ext} = 0$) are studied as a function of the nondimensional work of adhesion $\tilde{W}_{ad}$. For varying $\tilde{W}_{ad}$ two cases generally arise: 1) a unique stable solution branch and 2) bistable solution branches with an intermediate unstable branch. The solutions can be characterized by shell flatness or by potential, adhesive, or elastic energy, all of which are considered in the following analysis. Details of the separation profiles, adhesive tractions, and energy distributions are also discussed. A general feature of all the solutions is nonuniform separation and nonzero tractions at equilibrium.

3.1 Equilibrium Solution Paths Characterized by Shell Flatness

Equilibrium solutions characterized by the shell flatness parameter are plotted as a function of the nondimensional work of adhesion in Fig. 3 for various values of the curvature and range of interactions. The flatness parameter, which is defined in (13), has a value $\Phi=1$ for an undeformed configuration and a value $\Phi=0$ for a perfectly flat configuration. Although the latter state is unattainable for $\kappa \neq 0$ (see Sect. 2.3), states that approach $\Phi=0$ are always the most deformed (highest elastic energy) configurations. In all cases, turning or critical points ($\delta\Phi/\delta\tilde{W}_{ad} \to \infty$) indicate a change in stability. These points are referred to as the snap-in and snap-out transition values and they are tabulated in Table 2 for the short-range interactions $\tilde{\delta}_o$=1, 0.1, 0.01, and 0.001.

A key feature of the equilibrium curves is the emergence of bistable solutions for sufficiently large λ shells (at fixed $\tilde{\delta}_o$), whereas for smaller λ the solutions are unique. The values of λ at which bistable solutions appear depends on $\tilde{\delta}_o$. Deformation modes for long- and short-range adhesive interactions can differ substantially:

i) For relatively short-range interactions and small curvatures the solutions are unique and the shell flatness parameter varies monotonically with the load (e.g. $\tilde{\delta}_o$ = 1 and 0.1 with λ=1 in Figs. 3b,c). Alternatively, in the bistable regimes that occur at larger curvatures discontinuous snap-in and snap-out transitions are expected at the critical points $\tilde{W}_{ad}^{+}$ and $\tilde{W}_{ad}^{-}$ for continued loading and unloading, respectively. In particular, under increasing load the snap transitions result in the propagation of a nearly flat, central adhesion zone across the shell surface, and a corresponding decrease in Φ. The adhesion zone recedes upon unloading. The snap-in transition values $\tilde{W}_{ad}^{+}$ are more sensitive to changes in λ than $\tilde{\delta}_o$, whereas the snap-out transition values $\tilde{W}_{ad}^{-}$ depend on $\tilde{\delta}_o$, but are relatively insensitive to λ (see Table 2).

ii) For long-range interactions and relatively small curvature, for example $\tilde{\delta}_o$=10 with λ=1 and 6 in Fig. 3a, the shell flatness parameter varies monotonically with respect to load. However, at larger curvatures (λ=12 and 18) stable buckling occurring at the shell apex results in configurations that are concave-down in the interior and concave-up on the periphery, and a corresponding increase in the flatness parameter Φ. These wrinkles are flattened as the load is increased further. For relatively large curvatures (e.g. λ=18) an unstable buckling transition occurs at larger loads resulting in a second curvature inversion (concave-up in the interior and on the periphery, concave-down in between). Both the stable and unstable curvature inversions occur at relatively large values of $\tilde{W}_{ad}$ (note the scale of the abscissa in Fig. 3a).

The curvature inversions of the central region in *ii*) are qualitatively similar to the results of Komura et al. (2005) obtained for a tethered spring approximation of a closed spherical shell loaded by *long-range* adhesive interactions $H/\delta_o = \lambda/2\tilde{\delta}_o \approx 0.2-1.1$. However, the problems of interest in this study are associated with relatively short-range interactions. For example, in cell adhesion and wafer bonding this ratio takes a typical value that is on the order of 100-1000. Therefore, the remainder of this paper focuses on the solutions characteristic of *i*) above.

3.2 Potential, Elastic, and Adhesive Energy Paths

Although shell flatness is a measure of the overall deformation, it is not an indicator of global stability. For example, a flat configuration on the secondary solution branch can have a higher potential energy than a small deformation solution on the primary branch. In such a case the flat configuration is metastable, while the small deformation, lowest energy configuration is absolutely stable. With no external load ($\tilde{P}_{ext} = 0$) the potential energy of the system, defined by (2), includes only the adhesive energy U_a and the elastic energy U_e. In this case the reference potential energy $U_t = 0$ is taken as the undeformed, traction-free state $z = \infty$.

Typical variations of the potential, adhesive, and elastic energies with respect to the nondimensional work of adhesion are plotted in Fig. 4. Primary branch solutions are identified with relatively high adhesive energy and relatively low elastic energy (see Figs. 4b,c). Alternatively, secondary branch solutions are relatively low in adhesive energy and high in elastic energy. Since the secondary branch solutions are nearly flat configurations, the adhesive energy varies nearly in direct proportion to the work of adhesion and the elastic energy asymptotes to that of a flat configuration.

The potential energy landscape can be inferred from the equilibrium curves plotted in Fig. 4a. Schematic representations of the landscape in terms of the flatness measure Φ are given in Fig. 5. Although not drawn to scale in this schematic, the height of the barriers can be estimated from the potential energy of the unstable solution branches. In real systems these barriers can be lowered by imperfections and by *intermediate* nonaxisymmetric configurations that occur during the (dynamic) snap transitions (Budiansky, 1959). At a fixed $\tilde{\delta}_o$, equilibrium of relatively small λ shells corresponds to a single energy minimum (A) that progresses continuously toward lower potential energy states as $\tilde{W}_{ad}$ is increased. Alternatively, for large λ there is a unique energy minimum (A) for small $\tilde{W}_{ad}$, but at larger $\tilde{W}_{ad}$ a secondary minimum (B) develops corresponding to flatter configurations. At its initiation the secondary minimum (B) is high in potential energy (metastable), while the primary minimum (A) is low in potential energy (absolutely stable). As $\tilde{W}_{ad}$ is increased further, the relative depth of the two minima shift and eventually the secondary minimum (B) replaces (A) as the global minimum. With additional loading the primary minimum (A) is lost and the shell snaps into the low Φ configuration (B), which becomes a unique, stable solution. Similarly, upon unloading the stable configuration (B) is first absolutely stable, then metastable, and then lost, which initiates the snap-out transition to configuration (A).

3.3 Bending versus Stretching Modes of Deformation

The fraction of elastic energy due to stretching deformations is plotted in Fig. 4d. Bending deformations always dominate the elastic response of small λ shells, while membrane stresses play an important role for large λ, particularly for the flat configurations of the secondary branch. For large λ shells and short-range interactions the slightly deformed primary branch configurations typical of small $\tilde{W}_{ad}$ are dominated by bending, whereas for long-range interactions stretching can still be important. For example, with $\tilde{W}_{ad} = 0.01$ and $\lambda = 6$

stretching deformations account for about 40% of the elastic energy if $\tilde{\delta}_o$=1, but only about 0.2% if $\tilde{\delta}_o$=0.001. Similar results are also found for the larger curvature values λ=12 and 18.

Although nonaxisymmetric deformations can not be ruled out without further examination for the stretching dominated, high elastic energy states found for λ=12 and 18, results from previous studies suggest axisymmetric analyses are adequate for the geometric and material properties considered in this paper. For example, in the problem of snap-through buckling nonaxisymmetric states are predicted to occur near $\lambda = 15$ (Bushnell, 1985). However, in problems with adhesion the range of axisymmetric solutions is expected to be extended because there is an additional adhesive energy penalty from nonaxisymmetric separation profiles. Furthermore, for a discrete spring model of a complete spherical shell nonaxisymmetric solutions have been found for long-range interactions ($H/\delta_o \lesssim 1$), but for short-range interactions ($H/\delta_o >> 1$) the buckling modes are suppressed and flat centrally-bonded solutions prevail (Komura et al., 2005). Almost all solutions presented in this paper correspond to moderate λ and short-range interactions ($H/\delta_o >> 1$).

3.4 Separation Profiles, Adhesive Tractions, and Energy Distributions

Typical separation, traction, and adhesive energy profiles are plotted in Fig. 6 for both small curvature shells with moderate range adhesive interactions ($\lambda = 1$, $\tilde{\delta}_o = 0.1$) and for large curvature shells with relatively short range interactions ($\lambda = 12$, $\tilde{\delta}_o = 0.01$). The ratio H/δ_o is useful in characterizing these results, which in the first case (see Figs. 6a-c) has a value H/δ_o=10 and in the second case (see Figs. 6d-f) a value $H/\delta_o = 600$. Clearly in undeformed configurations the adhesive interactions can extend over a greater portion of the shell surface for H/δ_o=10 than for $H/\delta_o = 600$ (the range of interactions extends to about 10 δ_o).

Adhered configurations for either short- or long-range interactions can be distinguished by the spatial distributions of adhesive energy. In the former case the adhesive energy density $u_a \approx -W_{ad}$ over a central adhesion zone and $u_a \approx 0$ over the rest of the shell (see Fig. 6f). In the latter case no such partitioning is possible, since the adhesive energy is nonuniform over the entire shell surface (see Fig. 6c). The separation profiles (see Figs. 6a,d) that result in these energy distributions are described as follows: *i*) for short-range interactions a central adhesion zone develops with $z \approx \delta_o$, outside of which the deformation is driven by compatibility and *ii*) for long-range interactions the separation profiles are everywhere nonuniform. A notable exception to this classification is for short-range interactions and small $\tilde{W}_{ad}$, for which the central adhesion zone is not flat nor the adhesive energy uniform (e.g. $\tilde{W}_{ad}$=0.1 in Figs. 6d-f).

Tractions tend to be distributed over the entire shell surface for long-range interactions (see Fig. 6b), but for short-range interactions the tractions are localized to a small transition region (boundary layer) at the edge of the centrally adhered region (see Fig. 6e). In the latter case, the traction distribution is nearly statically equivalent to a concentrated adhesive couple, which is responsible for the steep variation in the moment at the adhesion front (see Fig. 7b). No steep variations in the moment distribution are observed for long-range interactions (see Fig. 7a).

Bistable adhesion states that are shown to exist for moderate work of adhesion and sufficiently large curvature can correspond to very different configurations despite having

comparable potential energies. An example is plotted in Fig. 8 for λ=6, $\tilde{\delta}_o$=0.1, and $\tilde{W}_{ad} = 0.21$. The lowest energy state $U_t = -0.08\pi a^2 W_{ad}$ exhibits a flat central adhesion zone, where the majority of deformation occurs (see Fig. 8d). For the metastable state $U_t = -0.06\pi a^2 W_{ad}$ the adhesion zone extends over a larger fraction of the shell surface, resulting in an increase in elastic energy that is partially offset by the reduction in adhesive energy. The unstable solution $U_t = 0.06\pi a^2 W_{ad}$ corresponds to a bonded central region that lies between the two stable solutions. As discussed in Sect. 3.2, the energy barrier in transitioning between absolutely stable and metastable states can be estimated from the unstable solution. For the case plotted in Fig. 8 the energy barrier in going from the stable to metastable state is $\Delta U_t = 0.14\pi a^2 W_{ad}$, while for the reverse transition $\Delta U_t = 0.12\pi a^2 W_{ad}$.

3.5 Discussion

The equilibrium states of adhered shell structures are difficult to determine due to the nonlinearities associated with both finite kinematics and adhesive loading. In general, the full nonlinear governing equations must be solved to determine the adhered states, which often are not unique. In the literature approximate analytic solutions have been constructed using linear bending theory and Griffith approximations (Seifert, 1991; Turner and Spearing, 2002; Freund and Yuan Lin, 2004; Graf et al., 2006), avoiding the complications of the full problem. Classification of solutions in terms of λ and in terms of the ratio $H/\delta_o = \lambda/2\tilde{\delta}_o$ is useful to characterize the complete solutions and to determine when these approximate solutions fail.

The dimensionless curvature λ distinguishes between solutions dominated by bending and those dominated by stretching. Small λ shells are dominated by linear bending. Conversely, for $\lambda \gtrsim 1$ the coupling between bending and stretching *must* be accounted for if accurate solutions are to be obtained. In the work of Graf et al. (2006) and in the continuum limit of Komura et al. (2005), the stretching contribution to the elastic energy is taken to have a quadratic dependence on the *linearized* in-plane strain tensor, which neglects coupling due to moderate rotations. Neglect of this coupling can result in significant errors in the elastic energy. Displacement fields of the nonlinear solutions can be used calculate the linearized elastic energy for (posteriori) error estimates. For example, the elastic energy of the primary branch solutions just prior to snap-in is overestimated in the linear theory by 1.5, 20, 40, and 52 percent for $\tilde{\delta}_o = 0.01$, and λ=1, 6, 12, and 18, respectively. Corresponding errors on the secondary solution branch with $\tilde{W}_{ad} = 2$ are 2, 45, 76, and 88 percent, respectively. These estimates are fairly insensitive to $\tilde{\delta}_o$ for the parameter values considered.

For the linear Griffith approximations to have validity the solutions must satisfy two requirements: *i*) linear bending theory must apply, which is satisfied if $\lambda \lesssim 1$ as discussed above, and *ii*) the total adhesive energy of the system must have the form $U_a = -\pi a_c{}^2 W_{ad}$, where a_c is the radius of a perfectly bonded, central adhesion zone. As shown by the adhesive energy profiles plotted in Fig. 6f, the latter condition is well approximated for short-range interactions ($H/\delta_o \gg 1$). However, breakdown of the Griffith approximation is expected at small $\tilde{W}_{ad}$, where no centrally flat adhesion zone can be identified. Although *ii*) is also well approximated

for large curvature shells, there is no clear way to construct a Griffith approximation from the nonlinear theory.

The analysis of this paper can be calibrated against the approximate solutions constructed by Turner and Spearing (2002) for linear bending ($\lambda \lesssim 1$) and short-range tractions ($H/\delta_o \gg 1$). Adapting their model to the current problem, snap-in and snap-out transitions are predicted to occur at $\tilde{W}_{ad}$=0.18, and 0.08, respectively, for $\nu = 0.3$ independent of λ or $\tilde{\delta}_o$. As anticipated, these values are very close to the values given in Table 2 for small curvature shells with short-range interactions. Despite good agreement in this narrow regime, for other values of λ and $\tilde{\delta}_o$ the linear Griffith approximations are inadequate.

4. Effect of Externally Applied Loads

In addition to adhesive tractions many systems of interest are also loaded externally during fabrication or in their natural state. External loading is also important for peeling or pull-off experiments used to measure the adhesive properties of an interface. The work done by applied loads enters the overall energy balance, altering both the equilibrium configurations and the energy distributions. In this section external loading by a uniform surface load (dead load) and a uniform edge load are considered, both applied in the vertical direction. An important aspect of this analysis is to show that not only is the magnitude of applied external load important, but also critically important is *how* the load is applied.

4.1 Uniform Surface Load

A uniform surface load (a body force) is applied to the adhered shell in the vertical direction, effectively adding to the adhesive tractions. The applied load P_{ext} is negative for compressive loading of the adhesive layer and positive for tensile loading (see Fig. 1). Under free-edge boundary conditions (8) - (10) static solutions only exist for external loading if $W_{ad} > 0$. Representative cross-sections of the equilibrium surface $\Phi(\tilde{W}_{ad}, \tilde{P}_{ext})$ are plotted in Fig. 9 for λ=6 with $\tilde{\delta}_o$=0.1 and 0.01. Figures 9a,b are equilibrium $\Phi - \tilde{W}_{ad}$ curves at fixed values of the normalized external load $\tilde{P}_{ext} = -0.01, -0.1$, and -1, which is defined in (12). Figures 9c,d are equilibrium $\Phi - P_{ext}$ curves at fixed values of the normalized work of adhesion $\tilde{W}_{ad}$ = 0.05, 0.1, and 1. Snap-in and snap-out $\tilde{W}_{ad}$ values corresponding to Figs. 9a,b are given in Table 3, whereas the critical points in Figs. 9c,d are given in Table 4. Details of these results follow.

For fixed geometric and material parameters compressive external loading enhances shell flattening, as shown in Figs. 9a,b. For relatively small pressures (e.g. $\tilde{P}_{ext} = -0.01$ and -0.1 for the case λ=6) the main characteristics of the $\Phi - \tilde{W}_{ad}$ equilibrium curves are not changed; there are bistable adhesion states for a given $\tilde{\delta}_o$ and sufficiently large λ. However, the corresponding snap-in and snap-out $\tilde{W}_{ad}$ transition values are reduced (see Table 3). Relatively large pressure (e.g. $\tilde{P}_{ext} = -1$ for $\lambda = 6$) can result in unique solutions corresponding to flat configurations, even if bistable states exist in the absence of external load.

Multiple solutions are also predicted under the conditions of constant work of adhesion and varying external load, as shown in Figs. 9c,d. In these figures $\delta\Phi/\delta P_{ext} > 0$ corresponds to stable solutions and $\delta\Phi/\delta P_{ext} < 0$ to unstable solutions. For $\tilde{W}_{ad}$=0.1 in Figs. 9c,d there are both bistable and unstable adhesion states. In contrast, for small work of adhesion (e.g. $\tilde{W}_{ad}$=0.05) the solutions are unique for all values of P_{ext}, and for large work of adhesion (e.g. $\tilde{W}_{ad}$=1) there is one stable branch corresponding to flat configurations and one unstable branch.

The effect of external load on the equilibrium configurations of the shell, i.e. the separation, traction, and energy distributions, are plotted in Fig. 10 for the parameters λ=6, $\tilde{\delta}_o$=0.1, and $\tilde{W}_{ad}$=0.1 with $\tilde{P}_{ext}$ = – 0.01, – 0.1, and –1. As shown clearly for the large compressive load values in Fig. 10b, the adhesive tractions on the flat central region of the shell are repulsive in order to satisfy equilibrium and, therefore, the separations are less than δ_o. The smaller separations increase the local adhesive energy density, as evident in Fig. 10c. Changes in the elastic energy fields correlate with increased shell flattening caused by the compressive load (see Fig. 10d).

4.2 Pull-Off Force: Surface versus Edge Loading

Pull-off occurs for load prescribed boundary conditions at the points on the loading curve for which no stable, higher Φ states exist. For example, consider the two cases $\tilde{\delta}_o$=0.1 and $\tilde{\delta}_o$=0.01 in Figs. 9c,d, respectively, with $\tilde{W}_{ad}$=0.1. In the first case of relatively long-range interactions, unloading from flat configurations results in a snap-out transition that, in the presence of moderate dissipation mechanisms (e.g. viscous drag), comes to equilibrium in a stable configuration. The solutions remain stable under continued load reductions until, under a small tensile load, pull-off occurs at the terminus (indicated by circles in Figs. 9c,d) of the stable equilibrium branch. In the second case, unloading from flat configurations results in pull-off directly from a small Φ state since there are no stable, higher Φ solutions for larger tensile load. Alternatively, when unloading from high Φ states pull-off occurs at the terminus of the solution branch, but at a much smaller tensile load than pull-off from the flat configuration (see Table 4 for comparisons between the critical values).

A uniform edge load is also applied to the spherical cap to investigate pull-off under an alternate external loading condition. The edge load corresponds to adding a shear force Q_o to the right-hand side of boundary condition (9) or equivalently adding the force $F = 2\pi a Q_o$ to the left-hand side of (11). For brevity, detailed analysis of the equilibrium profiles and traction distributions are not presented for this loading configuration. However, it is sufficient to note that the redistribution of adhesive tractions is concentrated near the shell boundary where the edge load is applied, in contrast to the more uniform redistribution in the case of a surface load.

Pull-off force calculations for both a uniform surface load and a uniform edge load are plotted in Fig. 11 for λ = 1, 6, 12, and 18 and the two values $\tilde{\delta}_o$=0.1, and 0.01. For all cases in this figure, pull-off occurs from a relatively flat configuration, as in the cases $\tilde{W}_{ad}$=1 in Figs. 9c,d. Evidently, the critical load required to separate the shell from a flat configuration depends dramatically on how the load is applied. In some cases the resultant pull-off force under edge loading can be more than an order of magnitude smaller than for surface loading. In addition,

the pull-off force is much more sensitive to λ and $\tilde{\delta}_o$ for edge loading than for surface loading. In fact, surface loading is shown to be relatively independent of both λ and $\tilde{\delta}_o$. At moderate to large $\tilde{W}_{ad}$ the pull-off force under edge loading varies nearly in direct proportion to the ideal interface strength $\pi a^2 \sigma_m$ (see Figs. 11c,d), although the proportionality depends on both λ and $\tilde{\delta}_o$. Conversely, for small $\tilde{W}_{ad}$ the correlation under edge loading is nonlinear. The important implication of this result is that the type of applied loading must be accounted for when deducing adhesive properties from experimentally measured pull-off force values. In all cases calculated pull-off forces are less than that of an ideal interface due to the release of stored elastic energy.

4.3 Discussion

By altering the equilibrium configurations at a local level, external loading can change the adhesive energy required for snap transitions and it can even induce such transitions. As may be expected, compressive loading reduces the snap-in and snap-out $\tilde{W}_{ad}$ values, while tensile loading increases them. Similarly, increasing $\tilde{W}_{ad}$ reduces the magnitude of compressive external load $\tilde{P}_{ext}$ required for snap-in and increases the magnitude of tensile load for snap-out or pull-off. As a result of the snap-transitions there is hysteresis in a bonding-unbonding process. The local equilibrium fields and, therefore, the pull-off forces are shown to depend strongly on how the external load is applied.

Application and subsequent removal of compressive load with the goal of inducing flat configurations can result in poor adhesion (metastable states). Depending on the geometry and on both the material and adhesive properties, load induced high energy states can result in spontaneous failure under external perturbations. Configurational robustness, measured by the height of the potential energy barrier between stable configurations, can be estimated from the potential energy of the unstable state (see Sect. 3.2). Typically maintaining a high work of adhesion comes at some cost, for example in wafer bonding surface contamination must be kept to a minimum. Estimates of the system robustness can be used to determine the best compromise between structural integrity and work of adhesion. For example, a work of adhesion below the snap-in transition value can be chosen such that, in conjunction with an external loading cycle, a robust, absolutely stable configuration is obtained.

5. Summary and Discussion

The adhesion of a shallow spherical cap to a rigid substrate is studied using the nonlinear shallow shell equations and a nonlinear adhesion law derived from Lennard-Jones interactions. Free-edge boundary conditions (or continuity for a closed shell) lead to equilibrium states with nonuniform energy distributions and nonzero tractions. In particular, when the ratio between the shell height and the range of the interactions is small the adhesive energy is nonuniformly distributed over the entire shell surface, whereas when this ratio is large the adhesive energy is roughly proportional to the area of an ideally bonded central region. In addition, the coupling between bending and stretching that arises due to the nonzero Gaussian curvature of the shell results in the development of membrane stresses during flattening deformations. This nonlinear coupling must be accounted for once the height to thickness ratio of the shell approaches unity. Together, these findings demonstrate that approximate solutions based on linear bending theory

and Griffith assumptions are applicable only in the case of small curvatures and short-range interactions.

Snap-in and snap-out adhesive transitions induced by both adhesive tractions and externally applied load are predicted for sufficiently large curvature shells with fixed material properties. Compressive external loading is shown to promote flat configurations and, when held constant, reduces the work of adhesion required for snap-in and snap-out transitions. Similarly, increased work of adhesion reduces the compressive external load required to initiate snap-in transitions and increases the tensile load required for snap-out or pull-off.

An important conclusion of this paper is that the pull-off force, which is generally not a direct measurement of the interface strength (see Figs. 9,11), depends not only on the geometric and material parameters of the shell, but also on the type of applied loading. The latter dependence may partly explain the discrepancy between the relatively large pull-off forces measured in single molecule experiments of receptor-ligand pairs compared to those obtained for adhered vesicles with the same receptor-ligand system (Guttenberg et al., 2000). For the latter case the measured pull-off force depends intimately on the mechanics of the vesicle in addition to the adhesive layer. Nevertheless, if δ_o is known, then the interface strength can be inferred from pull-off force measurements by comparison with the theoretically predicted values, for example, calculated in Fig. 11. Of course the dependence of σ_m on the receptor and ligand densities must be known in advance in order to calculate the strength of single bonds.

When bistable adhesion states exist energy loss occurs during complete (quasi-static) loading cycles. The dissipated energy can be calculated by considering variations of the potential energy (2) with respect to the load variables $\tilde{W}_{ad}$ and $\tilde{P}_{ext}$. The amount of hysteresis in a complete loading cycle depends on both the snap-in and snap-out transition values and the details of both the primary and secondary solution branches. The dissipation may have important implications for the cyclic adhesion of shell structures in MEMs devices and in the cyclic adhesion of certain biological cells (e.g. Lymphocytes) (Dustin and Springer, 1991; Gunzer et al., 2000). In both cases power must be supplied in excess of the loss.

Adhesion induced snap transitions could be used to experimentally measure the work of adhesion. For example, an array of caps could be manufactured with known geometric and material parameters that are identical except in their curvature. When adhered to a surface the different curvature caps will obtain different adhesion states. In this example, the largest curvature cap that exhibits a snap-in transition indicates a critical point $\tilde{W}_{ad}^{cr+}$ for the family of theoretical solution curves calculated for different curvatures. The material and geometric properties associated with this critical curvature shell can be used to deduce the work of adhesion. An estimate for δ_o is required in this procedure. Although similar to micro-cantilever arrays developed for measurement of the adhesive properties of metallic surfaces (Mastrangelo and Hsu, 1993; Maboudian and Howe, 1997), a benefit to this method is the large geometry changes associated with the snap transitions. Optical measurements of some shallow caps depend sensitively on geometry (Charnay et al., 2003), which make them ideal for determining the critical curvature.

In another example, single cell studies have observed an increase in projected cell area with increased surface densities of ligand, although a maximum projected area is reached (Engler et al., 2004). Increased ligand coating should result in more receptor-ligand interactions and, therefore, increased work of adhesion, at least until entropic penalties become important. The presented results show increased flattening with increased work of adhesion, which also

corresponds to increased projected area (results not shown), albeit the increase is small for the shallow cap. Of course many other factors are present in the experiments of Engler et al. (2004) on living cells.

The solutions presented in this investigation assume a uniform work of adhesion, which may depend on the concentration of certain adhesive or impurity species. If the concentrations are fixed uniformly on the surface then the equilibrium solution paths for varying $\tilde{W}_{ad}$ (e.g. Fig. 3) can be interpreted in terms of chemical concentrations. In the case of wafer bonding the solutions clearly indicate that large concentrations of impurities, for example water, can have a critical effect on the adhered configuration, particularly when the work of adhesion is close to the snap-in or snap-out transition values. More generally, the distribution of chemical species is nonuniform and coupled to the local mechanical fields (Xu Yan and Bassani, 1999; Mishin et al., 2002; Freund and Yuan Lin, 2004; Smith and Seifert, 2007). A detailed analysis of this mechano-chemical coupling will be given in a subsequent paper.

6. Acknowledgments

Support of the National Science Foundation Grant CTS-04-04259 and the Ashton Foundation is gratefully acknowledged.

7. Appendix

Numerical solutions of the governing equations (6) - (7), the compatibility condition (5), and boundary conditions (8) - (10) are obtained using finite difference methods. The derivative terms are approximated using five-point finite differences over a *nonuniform* grid and the integral term in (6) is approximated by a quadrature rule based on quadratic Lagrange interpolating polynomials. Solutions of the discretized equations are found using a continuation method that utilizes a tangent predictor step and a Gauss-Newton corrector step (Allgower and Georg, 2003). Details of the solution procedure are discussed below.

The governing equations are normalized by the nondimensional variables:

$$\tilde{z} = \frac{z}{H}, \quad \tilde{\psi} = \frac{a}{Et^3}\psi, \quad \tilde{\beta} = \frac{a}{H}\beta, \tag{A14}$$

along with the nondimensional geometric and load parameters:

$$\lambda = \frac{\kappa a^2}{t}, \quad \tilde{\delta}_o = \frac{\delta_o}{t}, \quad \tilde{W}_{ad} = \frac{W_{\mathrm{ad}}}{Et^3\kappa^2}, \quad \tilde{\sigma}_m = \frac{\sigma_m}{E\left(\kappa t\right)^2}, \quad \tilde{P}_{ext} = \frac{P_{ext}}{E\left(\kappa t\right)^2} \ . \tag{A15}$$

The nondimensional radial coordinate $\tilde{r} \in \left[0,1\right]$, defined as:

$$\tilde{r} = r/a \ , \tag{A16}$$

is discretized into n nodal points, with $\tilde{r}_k$ the position of the k^{th} node and $h_k = \tilde{r}_{k+1} - \tilde{r}_k$ the spacing between successive nodes. Boundary conditions (8) - (10) are enforced using a fictitious node $n+1$ located outside the solution domain at $\tilde{r}_{n+1} = 1 + 2h_{n-1} - h_{n-2}$, with the corresponding solution variables $\tilde{z}_{n+1}$, $\tilde{\psi}_{n+1}$ and $\tilde{\beta}_{n+1}$, determined by boundary conditions at the n^{th} node (Bushnell, 1985).

Five-point finite difference approximations for a nonuniformly spaced grid are used to approximate derivatives in the governing equations. Denoting the first and second finite difference operators by Δ_r and $\Delta_r{}^2$, respectively, the derivative approximations take the form:

$$\frac{dy}{dr} = \Delta_r y_k + O\left(\varepsilon_1 \left|\frac{d^5 y}{dr^5}\right|\right), \qquad \frac{d^2 y}{dr^2} = \Delta_r{}^2 y_k + O\left(\varepsilon_2 \left|\frac{d^5 y}{dr^5}\right|\right), \tag{A17}$$

where ε_1 and ε_2 are constants that depend on the mesh spacing and the derivatives are evaluated within the domain of the five grid points used in the approximation. On the interior nodes central difference approximations are used, whereas forward and backward difference approximations are used on the boundaries. For a uniformly spaced grid, both approximations are fourth order accurate on interior points, while for a nonuniformly spaced gird the accuracy of the second derivative is only third order. At the boundary points k = 1, 2, n, and n+1, the forward and backward difference approximations of the second derivative are always third order accurate, even for a uniformly spaced grid. The exact forms of the operators Δ_r and $\Delta_r{}^2$ are determined from standard analysis.

A discrete approximation to the integral term in (6) is constructed by integration of a quadratic Lagrange interpolating polynomial that is fit to the integrand y at three adjacent points. At the first grid point the polynomial is fit to function values at points $k = 1,2,3$, for the n^{th} grid point to the function values at $k = n, n-1, n-2$, and for all interior points k to the function values at $k-1, k, k+1$. The result is a third order accurate approximation I_r to the integral that takes the form:

$$\int_0^{\tilde{r}_k} y \, d\tilde{r}' = I_r y_k + O\left(\varepsilon_3 \frac{d^4 y}{dr^4}\right), \tag{A18}$$

where ε_3 is a constant that depends on the grid spacing and the derivative is evaluated within the domain $\left[0, \tilde{r}_k\right]$. Once again, the form of the operator I_r is determined from standard analysis.

With the derivative and integral operators defined above, the discrete form of governing equations (5) - (7) are given, respectively, as:

$$\Delta_r \tilde{z}_k - 2\tilde{r}_k + \tilde{\beta}_k = 0 \ , \tag{A19}$$

$$\frac{1}{12\left(1-\nu^2\right)}\left(\tilde{r}_k \, \Delta_r{}^2 \tilde{\beta}_k + \Delta_r \tilde{\beta}_k - \frac{\tilde{\beta}_k}{\tilde{r}_k}\right) + \Delta_r \tilde{z}_k \, \tilde{\psi}_k + 2\lambda\left(\tilde{\sigma}_m \, I_r\left(\tilde{r}_k f_k\right) + \frac{\tilde{p}_{ext}}{2}\tilde{r}_k{}^2\right) = 0 \,, \tag{A20}$$

$$\tilde{r}_k \, \Delta_r{}^2 \tilde{\psi}_k + \Delta_r \tilde{\psi}_k - \frac{1}{\tilde{r}_k}\tilde{\psi}_k - \frac{\lambda^2}{4}\left(2\tilde{r}_k \, \tilde{\beta} - \frac{1}{2}\tilde{\beta}^2\right) = 0 \,, \tag{A21}$$

where the discrete traction function f_k is given by:

$$f_k = -\frac{3\sqrt{3}}{2}\left[\left(\frac{2\tilde{\delta}_o}{\lambda \, \tilde{z}_k}\right)^3 - \left(\frac{2\tilde{\delta}_o}{\lambda \, \tilde{z}_k}\right)^9\right]. \tag{A22}$$

The discrete boundary conditions (8) - (10) follow directly:

$$\Delta_r{}^2 \tilde{\beta}_n - \nu \Delta_r \tilde{\beta}_n = 0 \ , \tag{A23}$$

$$\Delta_r{}^2 \tilde{\beta}_n + \Delta_r \tilde{\beta}_n - \tilde{\beta}_n = 0 , \tag{A24}$$

$$\tilde{\psi}_n = 0 \ . \tag{A25}$$

Symmetry conditions are imposed at the origin by replacing equations (A19) - (A21) for $k = 1$ with:

$$\tilde{\beta}_1 = 0 , \quad \Delta_r \tilde{z}_1 = 0 , \quad \tilde{\psi}_1 = 0 . \tag{A26}$$

The first two conditions impose symmetry of the vertical displacement and the third condition insures there is no radial displacement at the origin.

This nonlinear, coupled system of $n+1$ equations can be written in the form:

$$\mathbf{F}\left(\mathbf{y}, \tilde{W}_{ad}, \tilde{P}_{ext}, \lambda, \tilde{\delta}_o\right) = 0 , \tag{A27}$$

where $\mathbf{y} = \left[\tilde{z}_k, \tilde{\psi}_k, \tilde{\beta}_k\right]$ is the solution vector and the remaining load and geometrical parameters are fixed. In this study the equilibrium states are presented as a function of the loading parameters $\tilde{W}_{ad}$ and $\tilde{P}_{ext}$. However, the parameterization (A27) fails at critical (turning) points, and therefore, an augmented system of equations must be defined to trace the equilibrium paths with bistable solutions. Consider the two augmented systems of equations:

$$\hat{\mathbf{F}}_1\left(\hat{\mathbf{y}}_1, \tilde{P}_{ext}, \lambda, \tilde{\delta}_o\right) = 0 \ , \tag{A28}$$

$$\hat{\mathbf{F}}_2\left(\hat{\mathbf{y}}_2, \tilde{W}_{ad}, \lambda, \tilde{\delta}_o\right) = 0 \ , \tag{A29}$$

where the solution variables are $\hat{\mathbf{y}}_1 = \left[\tilde{z}_k, \tilde{\psi}_k, \tilde{\beta}_k, \tilde{W}_{ad}\right]$ and $\hat{\mathbf{y}}_2 = \left[\tilde{z}_k, \tilde{\psi}_k, \tilde{\beta}_k, \tilde{P}_{ext}\right]$. These underdetermined nonlinear systems of equations can be solved with the addition of a scalar constraint equation, for example a constraint limiting change of the most rapidly varying solution variable (parameter switching) (Rheinboldt, 1980). Alternatively, the properties of the Moore-Penrose inverse can be used to solve the underdetermined system of equations in an analogue to Newton's method, commonly called the Gauss-Newton method (Allgower and Georg, 1997; Allgower and Georg, 2003). For the current study, a variation of the Gauss-Newton method that relies on parameter switching (outlined in algorithm 10.2.10 of Allgower and Georg (2003)) is used to calculate the equilibrium solution curves.

Initiation of the continuation algorithm requires a starting solution, which is obtained by solving (A27) with a globally convergent Newton method (Press et al., 1992). To initiate the continuation algorithm for (A28), the starting solutions are calculated using either $\tilde{W}_{ad} = 1 \times 10^{-4}$ or $\tilde{W}_{ad} = 3$. In the first case the initial guess is that of an undeformed shell with apex separation $0.8\delta_o$, and in the second case the initial guess is that of a perfectly flat shell with separation $0.99\delta_o$. Similarly, to initiate the continuation algorithm for (A29) initial solutions are calculated using either $\tilde{P}_{ext} = 0$ or $\tilde{P}_{ext} = -\tilde{\sigma}_m$ with an undeformed or flat configuration used as an initial guess, respectively.

Due to the emergence of interior boundary layers, an adaptive grid refinement strategy is needed to ensure accurate solutions. At each step in the continuation algorithm the discrete

equations are solved twice. For the i^{th} step in the continuation algorithm, a solution $\bar{y}_k^i$ is obtained using the grid h_k^{i-1} of the previous step. This solution is used to calculate the location $\tilde{r}^{*i}$ where the solution variables vary most rapidly, from which a new grid h_k^i is constructed to ensure consistent solution accuracy. The governing equations are solved again on the new grid to obtain the stored solution y_k^i. Rapid convergence of the second solution is obtained using a piecewise cubic interpolation of $\bar{y}_k^i$ as the initial guess to obtain y_k^i. The mesh progresses smoothly with the solution as long as the step size in the continuation algorithm is sufficiently small.

A simple refinement strategy based on the work of Chong (1978) proved sufficient for this problem. An estimate for the magnitude of the derivatives inside the boundary layer is based on exponential solution growth $y = C\exp\left(r/\varepsilon\right)$:

$$\frac{d^n y}{d\tilde{r}^n} = O\left(\varepsilon^{-n}\right). \tag{A30}$$

With this estimate applied to the local error terms in (A17) and (A18) the grid spacing h^* required to maintain a set accuracy α is estimated from the test functions $\Delta_r \tilde{z}_k$, $\Delta_r \tilde{\beta}_k$, $\Delta_r \tilde{\psi}_k$, and $\Delta_r\left(r_k f_k\right)$ after each step. A minimum grid spacing h_{tol} is enforced.

A uniform grid consisting of n^* points with spacing $h_k = h^*$ is centered at the location $\tilde{r}^*$, which corresponds to the location of the maximum derivative determined from the test functions above. Outside the boundary layer the spacing is increased according to $h_{I\pm\left(n^*/2+k\right)} = h^*\left(1+\theta\right)^k$, where I is the grid number at $\tilde{r}^*$, and θ determines the rate of increase. Derivatives outside the boundary layer are estimated to be $O(1)$ and, therefore, a maximum gird spacing of $\alpha^{1/3}$ insures an estimate consistent with the error inside the boundary layer. In the results presented $\alpha = 1\times10^{-3}$, $\theta = 1.5 - 2.5$, and the maximum gird spacing is $0.1\alpha^{1/3}$. The minimum spacing estimated by the test functions is generally conservative, so the computation time can be decreased by setting $h_{tol} = 5\times10^{-4}$ - 1×10^{-5}, which still maintains good convergence.

8. Figures

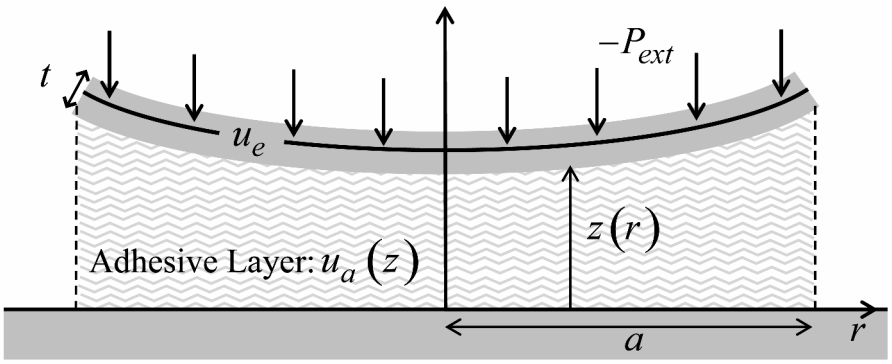

Figure 1. Thermodynamic system comprised of a shallow spherical shell that interacts with an adhesive layer and a rigid substrate at fixed external load.

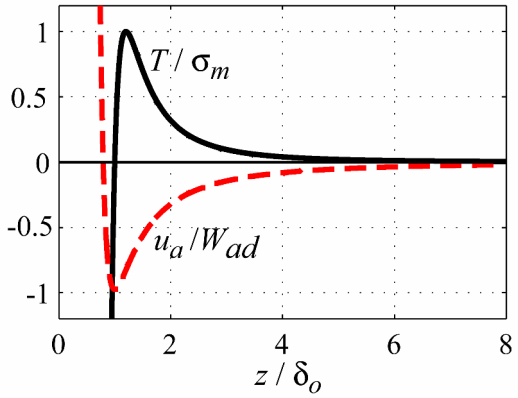

Figure 2. Adhesive energy density and corresponding tractions as a function of separation, as given by (4).

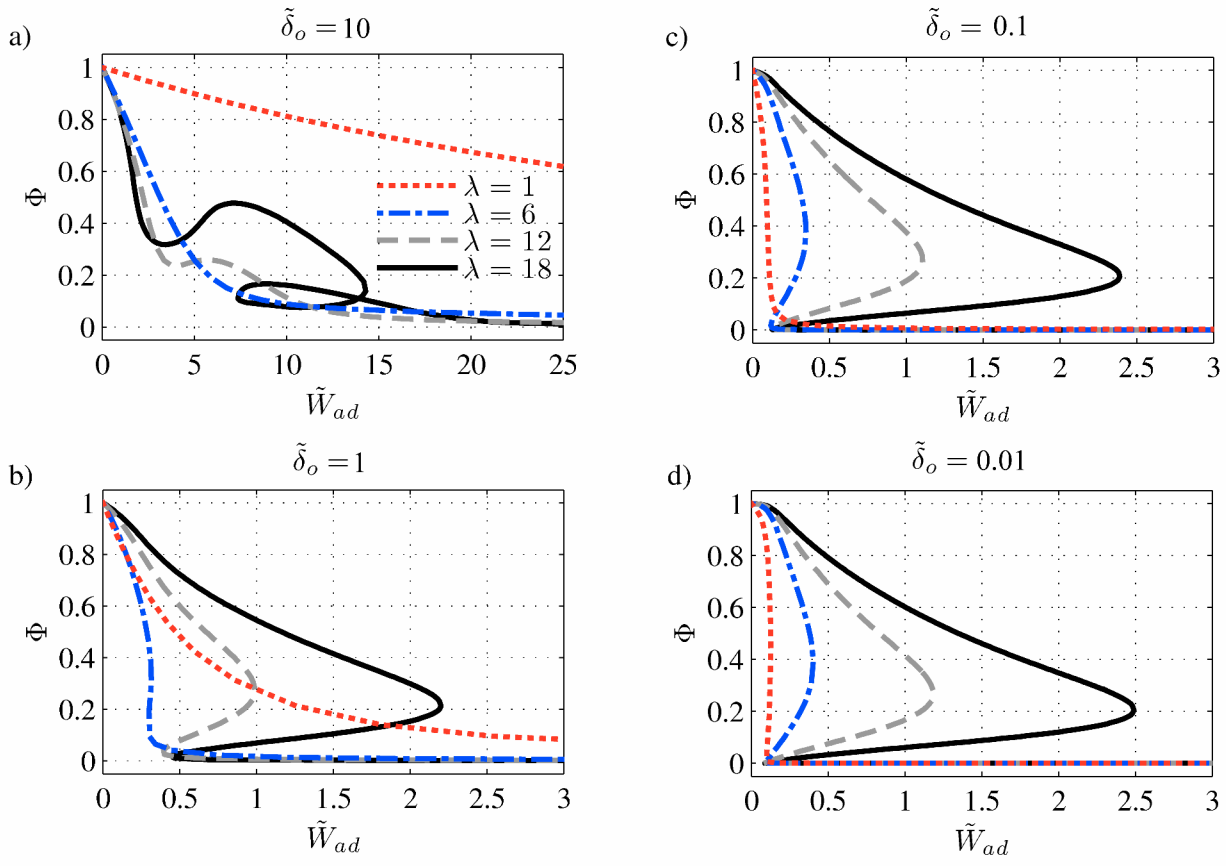

Figure 3. Shell flatness plotted as function of the nondimensional work of adhesion.

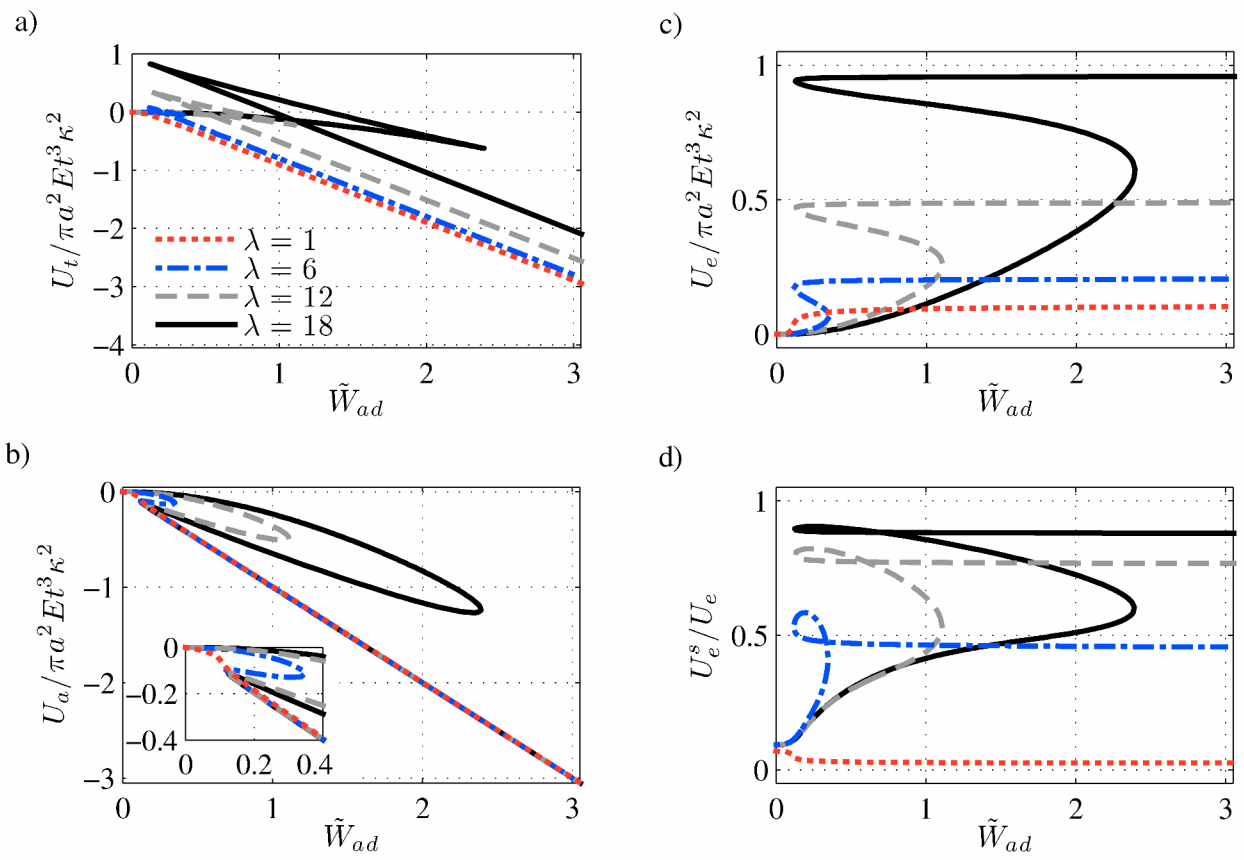

Figure 4. Total a) potential, b) adhesive, and c) elastic energies, and d) the fraction of elastic energy due to stretching deformations plotted as a function of the nondimensional work of adhesion for $\tilde{\delta}_o$ =0.1.

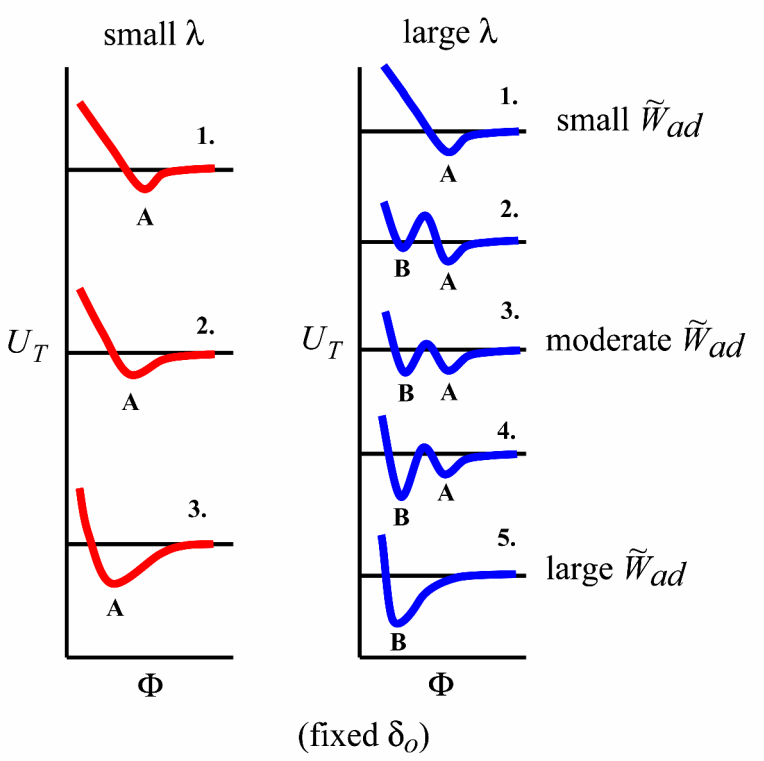

Figure 5. Schematic of the potential energy landscape characterized by the shell flatness parameter.

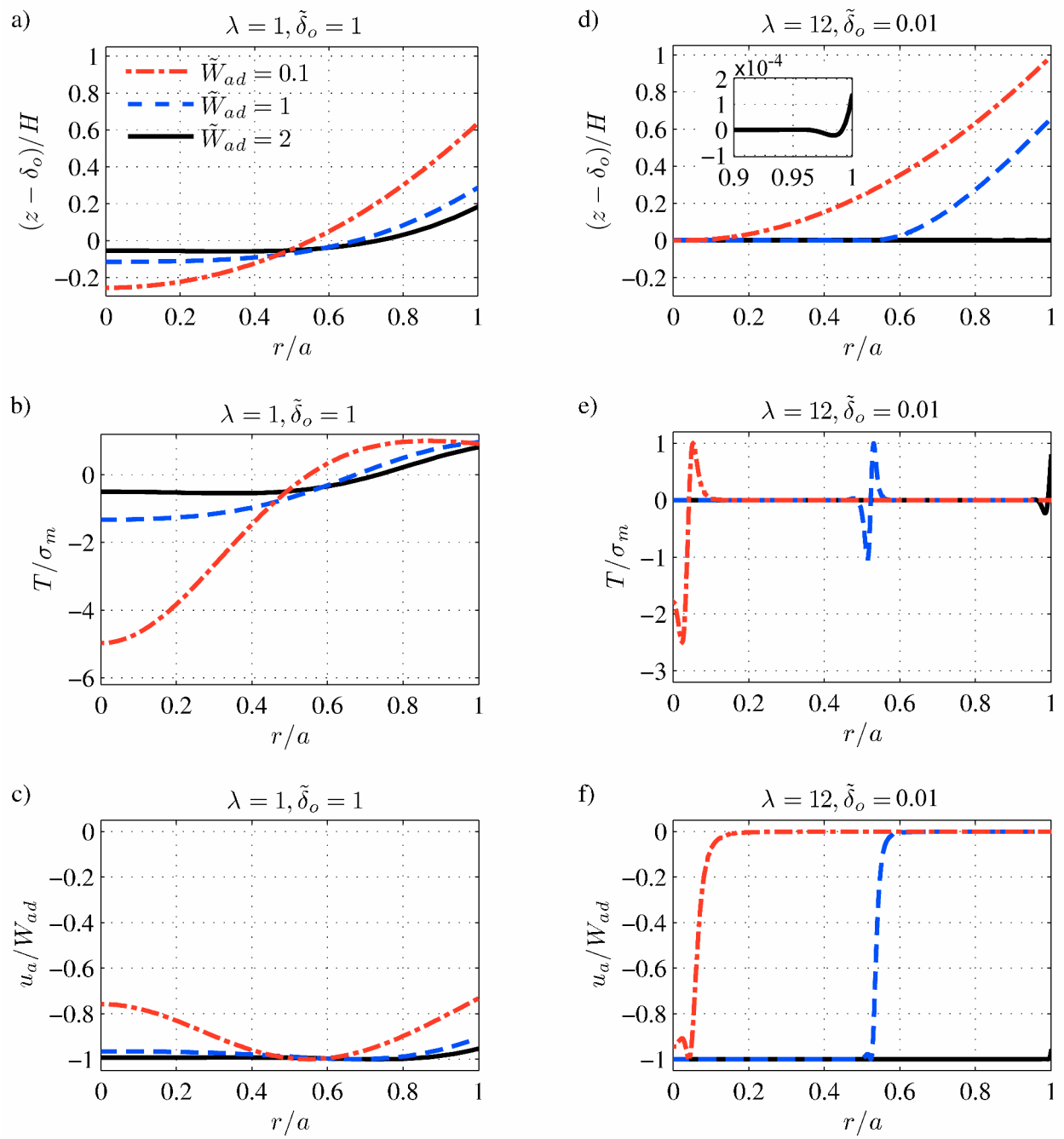

Figure 6. a,d) Separation, b,e) traction, and c,f) adhesive energy profiles.

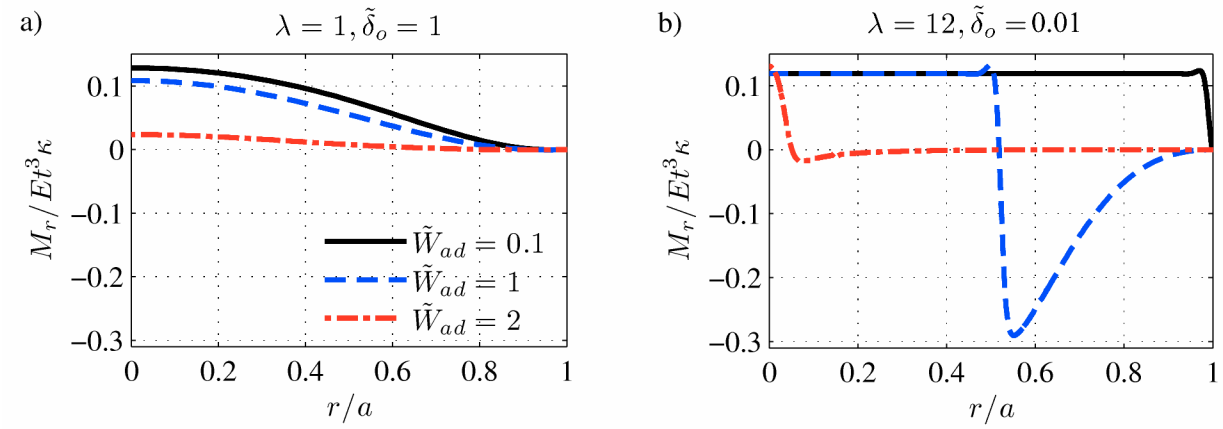

Figure 7. Radial moment as a function of the radial coordinate.

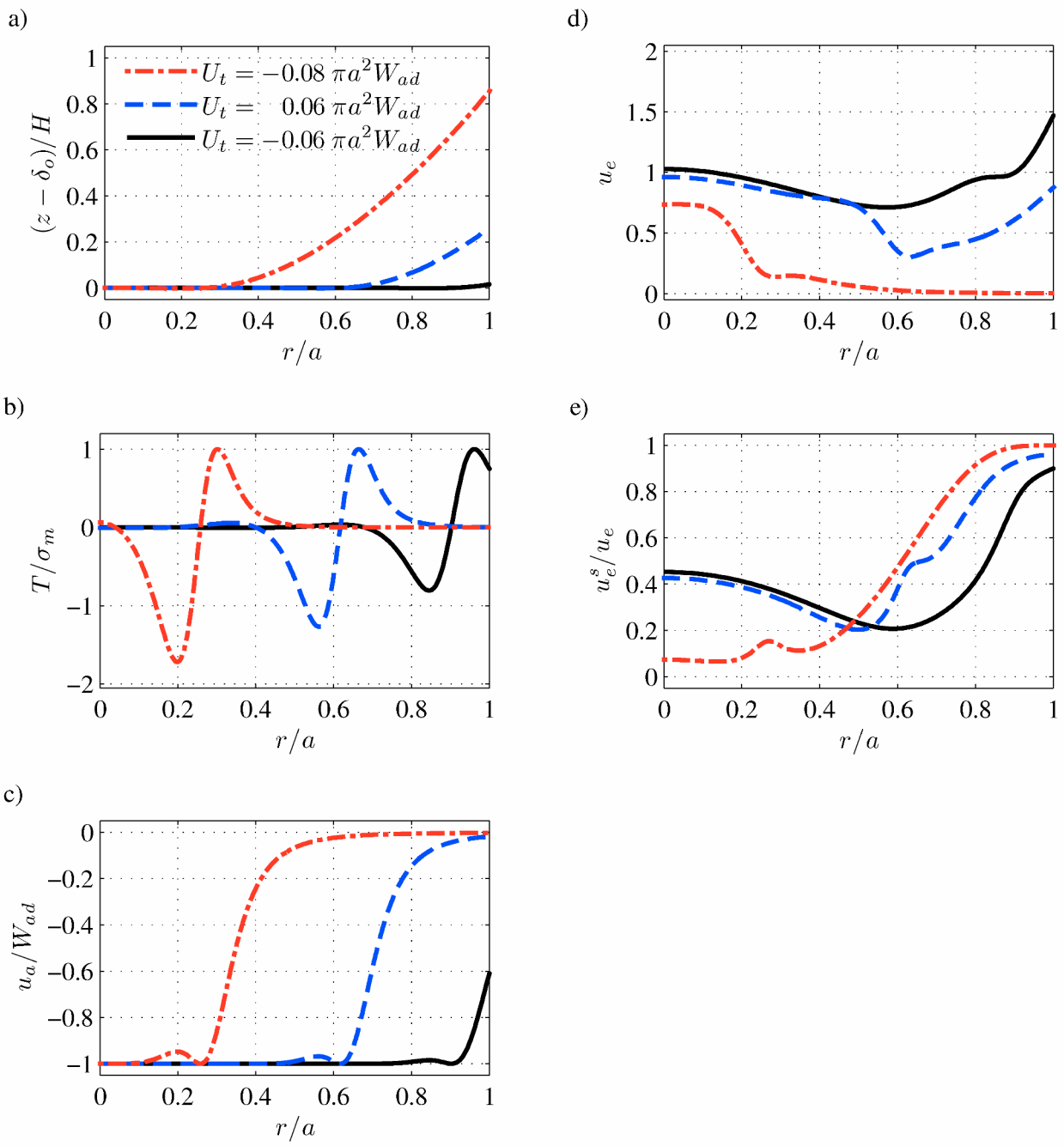

Figure 8. Bistable and unstable adhesion states for a fixed nondimensional work of adhesion $\tilde{W}_{ad}$ =0.21 with λ =6, and $\tilde{\delta}_o$ =0.1. The dash-dotted (red) and solid (black) lines correspond to stable configurations, whereas the dashed (blue) lines correspond to an unstable configuration.

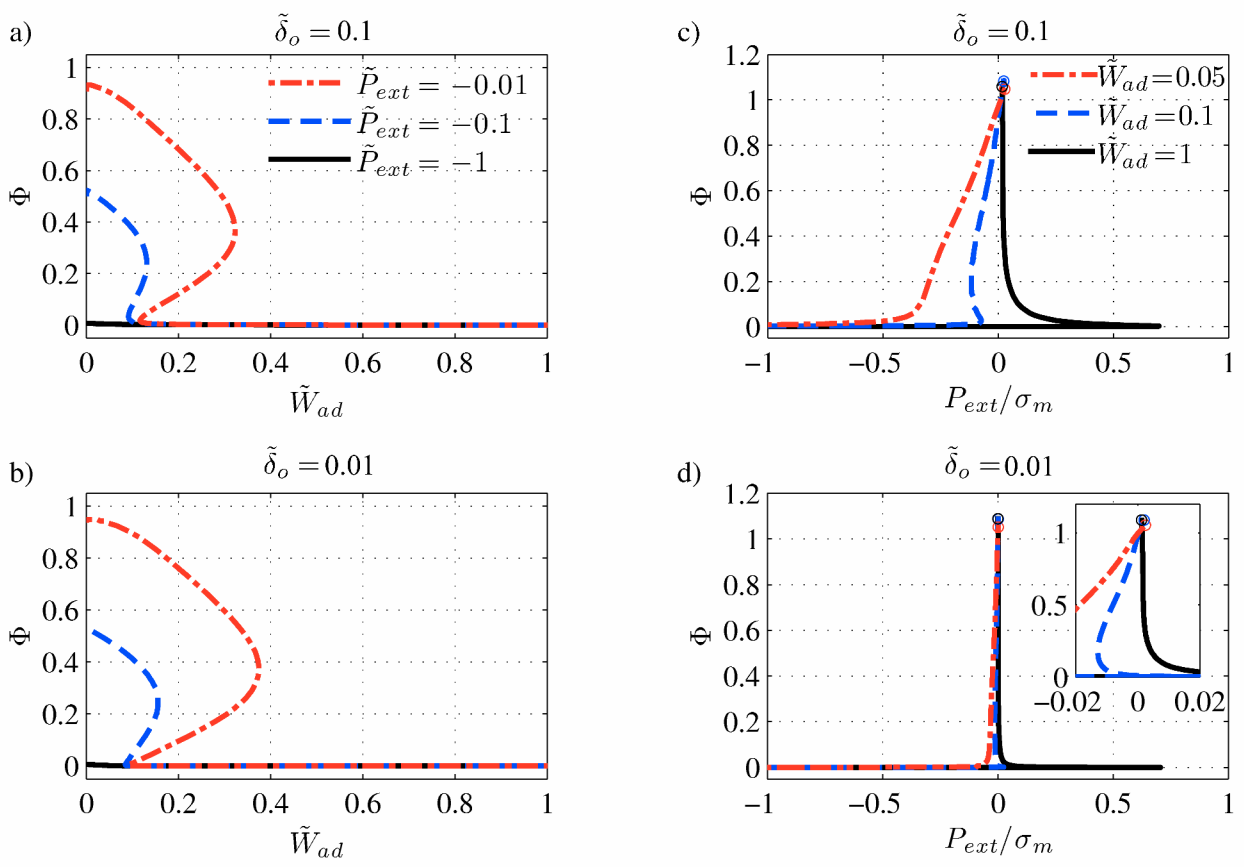

Figure 9. The effect of uniform surface loads on the adhesion state as measured by the shell flatness parameter for λ =6.

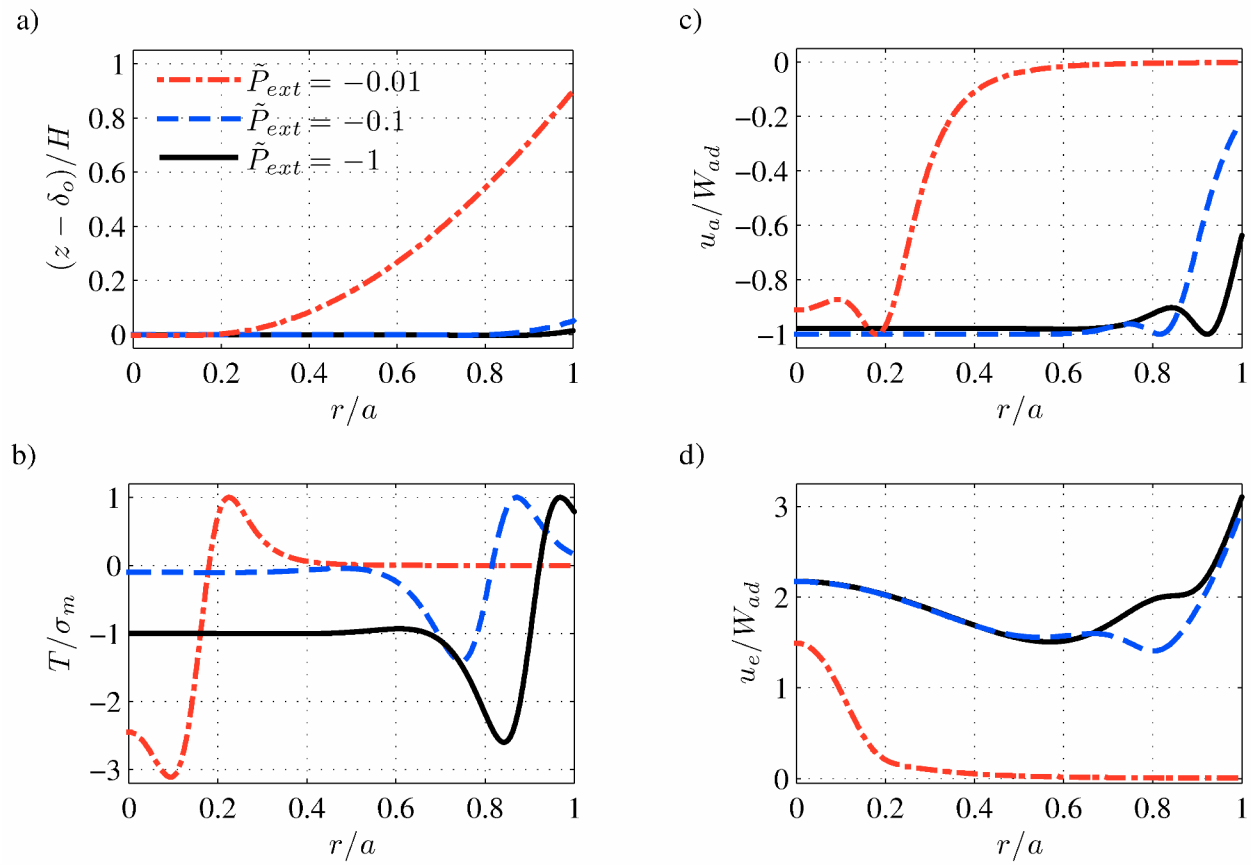

Figure 10. The effect of uniform surface loads on the a) separation, b) traction, c) adhesive energy, and d) elastic energy fields for λ =6, $\tilde{\delta}_o$ =0.1, and $\tilde{W}_{ad}$ =0.1.

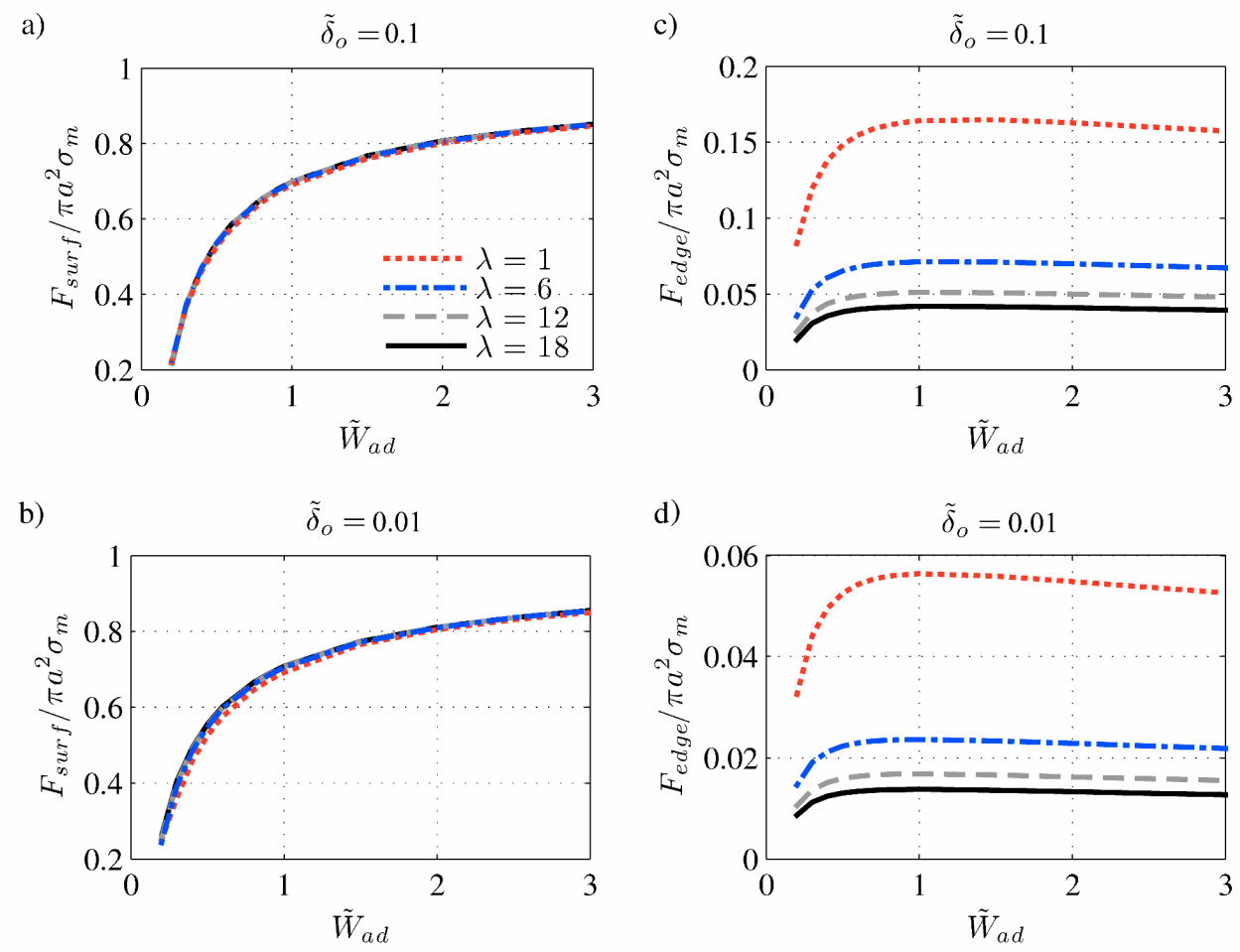

Figure 11. Calculated pull-off force for a,b) uniform surface loading, and c,d) uniform edge loading.

9. Tables

	Wafer Bonding	Gold Nanocaps	Cell Adhesion	Lipid Bilayer
$E\left(\mathrm{N/m^2}\right)$	150×10^{9} c	69.1×10^{6} e	1×10^{3} g	8×10^{6} k
$t\left(\mathrm{m}\right)$	1×10^{-3} c	12.5×10^{-9} f	0.4×10^{-6} h	4×10^{-9}
$a\left(\mathrm{m}\right)$	50×10^{-3} c	55×10^{-9} f	10×10^{-6}	1×10^{-3}
$\kappa\left(\mathrm{m^{-1}}\right)$	3×10^{-2} c	20×10^{6} f	1×10^{5}	1×10^{3}
$H\left(\mathrm{m}\right)$[a]	38×10^{-6}	303×10^{-6}	10×10^{-6}	1×10^{-3}
$W_{ad}\left(\mathrm{J/m^2}\right)$	40×10^{-3} c	2 d	20×10^{-6} i	20×10^{-6} i
$\delta_o\left(\mathrm{m}\right)$	0.15×10^{-9} d	0.18×10^{-9} d	15×10^{-9} j	10×10^{-9} l
$\sigma_m\left(\mathrm{N/m^2}\right)$[b]	410×10^{6}	11.4×10^{9}	2.1×10^{3}	2.1×10^{3}
$\tilde{\delta}_o$	1×10^{-7}	1×10^{-2}	3.75×10^{-2}	2.5
λ	0.08	4.84	25	2.5×10^{5}
$\tilde{W}_{ad}$	0.30	0.04	31	1×10^{7}

Table 1. Typical geometric and material parameters for adhesion of wafers, nanocaps, biological cells, and lipid membranes. a. For the wafer and gold nanocap shell height is calculated using the given system parameters and the shallow cap approximation $H=\kappa a^2/2$, while for the cell and lipid bilayer the height is set equal to the estimated radius for a spherical geometry; b. Maximum stress is calculated using the given system parameters and (4); c. Turner and Spearing (2002); d. Yu and Polycarpou (2004); e. Salvadori et al. (2003); f. Charnay et al. (2003); g. Pesen and Hoh (2005); h. Estimated thickness of the actin cortex from Lang et al. (2000) and Pesen and Hoh (2005); i. Simson et al. (1998); j. Izzard and Lochner (1976); k. Estimated from the membrane bending modulus $D=1.2\times10^{-19}\,N\cdot m$ (Secomb, 1988) using the shell bending modulus relation $D=Et^3/12\left(1-\nu^2\right)$ with the given vesicle dimensions and a Poisson's ratio $\nu=0.3$; l. Sackmann and Bruinsma (2002).

	$\tilde{\delta}_o = 1$	0.1	0.01	0.001
$\lambda = 1$	$-/-$	$-/-$	$0.12/0.10$	$0.16/0.09$
6	$0.32/0.30$	$0.35/0.12$	$0.40/0.09$	$0.42/0.08$
12	$0.99/0.39$	$1.11/0.13$	$1.18/0.09$	$1.21/0.08$
18	$2.20/0.45$	$2.39/0.13$	$2.49/0.09$	$2.52/0.08$

Table 2. Snap-in/out $\tilde{W}_{ad}$ transition values in the absence of external load ($\tilde{P}_{ext}$ =0).

	$\tilde{\delta}_o = 0.1$	0.01
$\tilde{P}_{ext} = -0.01$	$0.32/0.12$	$0.37/0.09$
-0.1	$0.13/0.09$	$0.16/0.08$
-1	$-/-$	$-/-$

Table 3. Snap-in/out $\tilde{W}_{ad}$ transition values for external loading and λ =6, corresponding to Figs. 9a,b.

	$\tilde{\delta}_o = 0.1$	0.01
$\tilde{W}_{ad} = 0.05$	$-/-/0.028/-$	$-/-/0.002/-$
0.1	$-0.117/-0.073/0.025/-$	$-0.01/-/0.002/0.025$
1	$-/-/-/0.700$	$-/-/-/0.706$

Table 4. Critical values of P_{ext}/σ_m for snap-in/snap-out/pull-off from terminus of stable equilibrium states/pull-off from relatively flat configurations, corresponding to Figs. 9c,d for λ =6.

10. References

Allgower, E. L., Georg, K., 1997. Numerical path following. In: Ciarlet, P.G. and Lions, J.L. (Eds.), Handbook of Numerical Analysis, vol. 5. North Holland: Elsevier Science, pp. 3-207.

Allgower, E. L., Georg, Kurt., 2003. Introduction to Numerical Continuation Methods. Society for Industrial and Applied Mathematics, Philadelphia, PA, USA.

Boal, David., 2002. Mechanics of the Cell. Cambridge University Press, Cambridge.

Boulbitch, A., Simson, R., Simson, D.A., Merkel, R., Hackl, W., Barmann, M., Sackmann, E., 2000. Shape instability of a biomembrane driven by a local softening of the underlying actin cortex. Physical Review E 62 (3), 3974-3985.

Budiansky, B., 1959. Buckling of Clamped Shallow Spherical Shells. In: Koiter, W.T. (Ed.), Proceedings of IUTAM Symposium on the Theory of Thin Elastic Shells, pp. 64-94.

Budiansky, B., 1968. Notes on nonlinear shell theory. ASME Journal of Applied Mechanics 35 (2), 393-430.

Bushnell, D., 1985. Computerized buckling analysis of shells. Martinus Nijhoff Publishers, Dordrecht.

Cahn, J. W., 1979. Thermodynamics of Solid and Fluid Surfaces. In: Johnson, W.C., Blakely J.M. (Eds.). Interfacial Segregation. AME, Metals Park, OH, pp. 3.

Charnay, C., Lee, A., Man, S.Q., Moran, C.E., Radloff, C., Bradley, R.K., Halas, N.J., 2003. Reduced symmetry metallodielectric nanoparticles: chemical synthesis and plasmonic properties. Journal of Physical Chemistry B 107 (30), 7327-7333.

Chen, J., Ding, H., Wang, J., Shao, L., 2004. Preparation and characterization of porous hollow silica nanoparticles for drug delivery application. Biomaterials 25 (4), 723-727.

Chong, T.H., 1978. A variable mesh finite difference method for solving a class of parabolic differential equations in one space variable. SIAM Journal on Numerical Analysis 15 (4), 835-857.

Dobereiner, H.G., Dubin-Thaler, B., Giannone, G., Xenias, H.S., Sheetz, M.P., 2004. Dynamic phase transitions in cell spreading. Physical Review Letters 93 (10), 108105-108110.

Dustin, M.L., Springer, T.A., 1991. Role of Lymphocyte Adhesion Receptors in Transient Interactions and Cell Locomotion. Annual Review of Immunology 9, 27-66.

Engler, A., Bacakova, L., Newman, C., Hategan, A., Griffin, M., Discher, D., 2004. Substrate compliance versus ligand density in cell on gel responses. Biophysical Journal 86 (1), 617-628.

Evans, E. A., Skalak, R., 1980. Mechanics and thermodynamics of biomembranes. CRC Press, Boca Raton, Florida.

Freund, L.B., Yuan Lin., 2004. The role of binder mobility in spontaneous adhesive contact and implications for cell adhesion. Journal of the Mechanics and Physics of Solids 52 (11), 2455-2472.

Galbraith, C.G., Yamada, K.M., Sheetz, M.P., 2002. The Relationship between Force and Focal Complex Development. Journal of Cell Biology 159 (4), 695-705.

Graf, P., Finken, R., Seifert, U., 2006. Adhesion of Microcapsules. Langmuir 22 (17), 7117-7119.

Griffith, A.A., 1921. The phenomena of rupture and flow in solids. Philosophical Transactions of the Royal Society of London A 221, 163-197.

Guggenheim, E. A., 1993. Thermodynamics: An Advanced Treatment for Chemists and Physicists. North Holland: Elsevier Science.
Gunzer, M., Schafer, A., Borgmann, S., Grabbe, S., Zanker, K.S., Brocker, E.B., Kampgen, E., Friedl, P., 2000. Antigen presentation in extracellular matrix: interactions of T cells with dendritic cells are dynamic, short lived, and sequential. Immunity 13 (3), 323-332.
Guttenberg, Z., Bausch, A.R., Hu, B., Bruinsma, R., Moroder, L., Sackmann, E., 2000. Measuring ligand-receptor unbinding forces with magnetic beads: Molecular leverage. Langmuir 16 (23), 8984-8993.
Helfrich, W., 1973. Elastic properties of lipid bilayers: theory and possible experiments. Zeitschrift für Naturforschung C 28 (11), 693-703.
Hutchinson, J.W., 1967. Imperfection sensitivity of externally pressurized spherical shells. ASME Journal of Applied Mechanics 34 (1), 49-55.
Israelachvili, J.N., Tabor, D., 1972. The measurement of van der Waals dispersion forces in the range 1.5 to 130 nm. Proceedings of the Royal Society of London, Series A 331 (1584), 19-38.
Israelachvilli, Jacob N., 1985. Intermolecular and Surface Forces: With Applications in Colloidal and Biological Systems. Academic Press, London.
Izzard, C.S., Lochner, L.R., 1976. Cell-to-substrate contacts in living fibroblasts: an interference reflexion study with an evaluation of the technique. Journal of Cell Science 21 (1), 129-159.
Klein, J., 1982. Forces between two polymer layers absorbed at a solid-liquid interface in a poor solvent. Advances in Colloid and Interface Science 16, 101-115.
Komura, S., Tamura, K., Kato, T., 2005. Buckling of spherical shells adhering onto a rigid substrate. European Physical Journal E 18 (3), 343-58.
Lang, T., Wacker, I., Wunderlich, I., Rohrbach, A., Giese, G., Soldati, T., Almers, W., 2000. Role of actin cortex in the subplasmalemmal transport of secretory granules in PC-12 cells. Biophysical Journal 78 (6), 2863-2877.
Leckband, D.E., Israelachvili, J.N., Schmitt, F.J., Knoll, W., 1992. Long-range attraction and molecular rearrangements in receptor-ligand interactions. Science 255 (505), 1419-1421.
Leckband, D.E., Schmitt, F.J., Israelachvili, J.N., Knoll, W., 1994. Direct force measurements of specific and nonspecific protein interactions. Biochemistry 33 (15), 4611-4624.
Leckband, D., Israelachvili, J., 2001. Intermolecular forces in biology. Quarterly Reviews of Biophysics 34 (2), 105-267.
Love, J.C., Gates, B.D., Wolfe, D.B., Paul, K.E., Whitesides, G.M., 2002. Fabrication and wetting properties of metallic half-shells with submicron diameters. Nano Letters 2 (8), 891-894.
Maboudian, R., Howe, R.T., 1997. Critical review: Adhesion in surface micromechanical structures. Journal of Vacuum Science and Technology B 15 (1), 1-20.
Mastragelo, C.H., Hsu, C.H., 1993. Mechanical stability and adhesion of microstructures under capillary forces-Part I: basic theory. Journal of Microelectromechanical Systems 2 (1), 33-43.
Mastrangelo, C.H., Hsu, C.H., 1993. Mechanical stability and adhesion of microstructures under capillary forces-Part II: Experiments. Journal of Microelectromechanical Systems 2 (1), 44-55.
Maugis, D., 2000. Contact, Adhesion and Rupture of Elastic Solids. Springer-Verlag, Berlin.
Mirza, A.R., Ayon, A.A., 1999. Silicon wafer bonding for MEMS manufacturing. Solid State Technology 42 (8), 73-74.

Mishin, Y., Sofronis, P., Bassani, J.L., 2002. Thermodynamics and kinetic aspects of interfacial decohesion. Acta Materialia 50 (14), 3609-3622.
Muller, V.M., Deryagin, B.V., Toporov, Y.P., 1983. Force of adhesion of a sufficiently rigid spherical elastic particle to a plane. Colloid Journal of the USSR 45 (3), 397-402.
Niordson, F., 1985. Shell Theory. North Holland: Elsevier Science.
Pesen, D., Hoh, J.H., 2005. Micromechanical architecture of the endothelial cell cortex. Biophysical Journal 88 (1), 670-679.
Press, William H., Teukolsky, Saul A., Vetterling, William T., Flannery, Brian P., 1992. Globally Convergent Methods for Nonlinear Systems of Equations. In: Numerical Recipes in Fortran. Cambridge University Press, Cambridge, pp. 383-393.
Reinhart-King, C.A., Dembo, M., Hammer, D.A., 2005. The dynamics and mechanics of endothelial cell spreading. Biophysical Journal 89 (1), 676-689.
Reissner, E., 1958. Symmetric Bending of Shallow Shells of Revolution. Journal of Mathematics and Mechanics 7 (2), 121-140.
Reissner, E., 1950. On axisymmetrical deformations of thin shells of revolution. In: Proceedings of the Symposium in Applied Mathematics, vol. 3. McGraw-Hill, pp. 231-247.
Rheinboldt, W.C., 1980. Solution fields of nonlinear equations and continuation methods. SIAM Journal on Numerical Analysis 17 (2), 221-237.
Sackmann, E., Bruinsma, R.F., 2002. Cell adhesion as wetting transition. Chemphyschem 3 (3), 262-269.
Salvadori, M.C., Brown, I.G., Vaz, A.R., Melo, L.L., Cattani, M., 2003. Measurement of the elastic modulus of nanostructured gold and platinum thin films. Physical Review B 67 (15), 153404-153410.
Sanders, J., J.L., 1963. Nonlinear theories for thin shells. Quarterly of Applied Mathematics 21 (1), 21-36.
Secomb, T.W., 1988. Interaction between bending and tension forces in bilayer membranes. Biophysical Journal 54 (4), 743-746.
Seifert, U., 1991. Adhesion of vesicles in two dimensions. Physical Review A 43 (12), 6803-6814.
Simson, R., Wallraft, E., Faix, J., Niewoehner, J., 1998. Membrane Bending Modulus and Adhesion Energy of Wild-Type and Mutant Cells of Dictyostelium Lacking Talin or Cortexillins. Biophysical Journal 74 (1), 514-522.
Smith, A.S., Lorz, B.G., Seifert, U., Sackmann, E., 2006. Antagonist-induced deadhesion of specically adhered vesicles. Biophysical Journal 90 (3), 1064-1080.
Smith, A.S., Seifert, U., 2007. Vesicles as a model for controlled (de-) adhesion of cells: a thermodynamic approach. Soft Matter 3 (3), 275-289.
Stoker, J. J., 1969. Differential Geometry. John Wiley & Sons, Inc., New York.
Tamura, K., Komura, S., Kato, T., 2004. Adhesion induced buckling of spherical shells. Journal of Physics: Condensed Matter 16 (39), 421-428.
Taunton, H.J., Toprakcioglu, C., Fetters, L.J., Klein, J., 1988. Forces between surfaces bearing terminally anchored polymer-chains in good solvents. Nature 332 (6166), 712-714.
Tsui, T.Y., Vlassak, J.J., McKerrow, A.J., 2006. The effect of water diffusion on the adhesion of organosilicate glass film stacks. Journal of the Mechanics and Physics of Solids 54 (5), 887-903.
Turner, K.T., Spearing, S.M., 2002. Modeling of direct wafer bonding: effect of wafer bow and etch patterns. Journal of Applied Physics 92 (12), 7658-7666.

Wan, F.Y.M., Weinitschke, H.J., 1988. On shells of revolution with the Love-Kirchhoff hypotheses. Journal of Engineering Mathematics 22 (4), 285-334.
Weinitschke, H.J., 1958. On nonlinear theory of shallow spherical shells. Journal of the Society for Industrial and Applied Mathematics 6 (3), 209-232.
Wong, J.Y., Kuhl, T.L., Israelachvili, J.N., Mullah, N., Zalipsky, S., 1997. Direct measurement of a tethered ligand-receptor interaction potential. Science 275 (5301), 820-822.
Xu Yan, Bassani, J.L., 1999. A steady-state model for diffusion-controlled fracture. Materials Science and Engineering A 260 (1), 48-54.
Yu, N., Polycarpou, A.A., 2004. Adhesive contact based on the Lennard-Jones potential: A correction to the value of the equilibrium distance as used in the potential. Journal of Colloid and Interface Science 278 (2), 428-435.

Figure(s)

Click here to download high resolution image

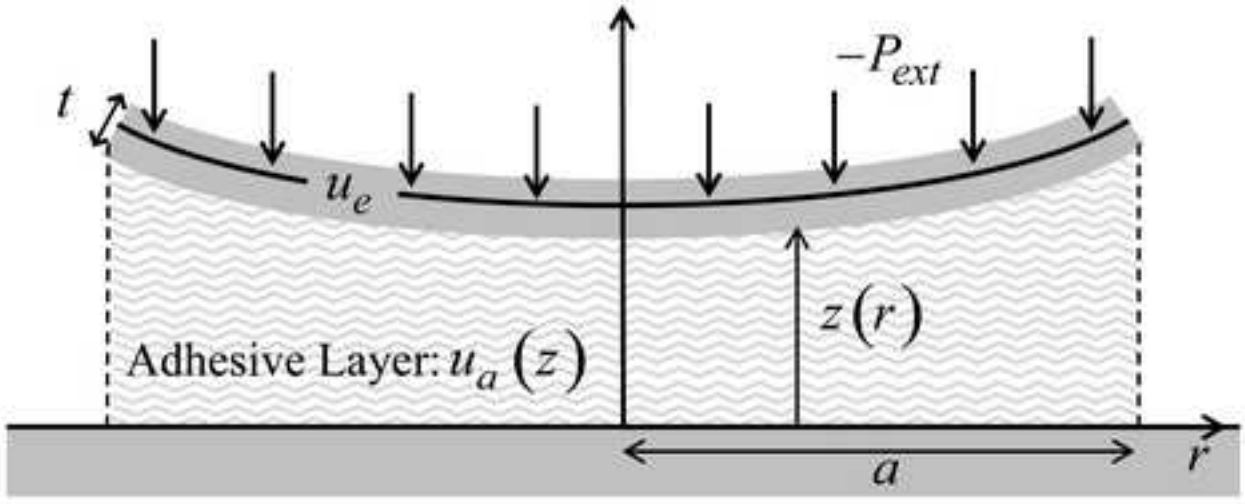

Figure(s)
Click here to download high resolution image

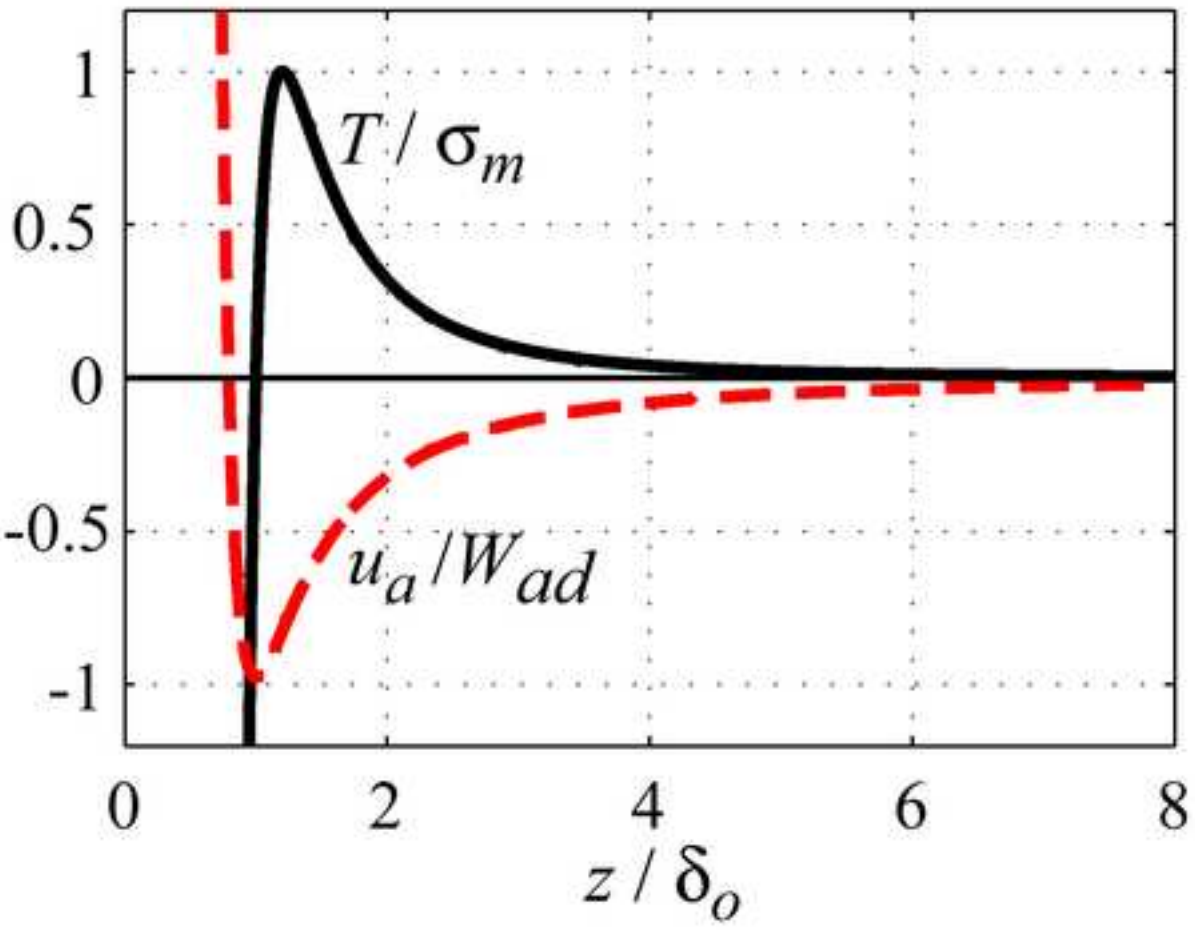

Figure(s)

Click here to download high resolution image

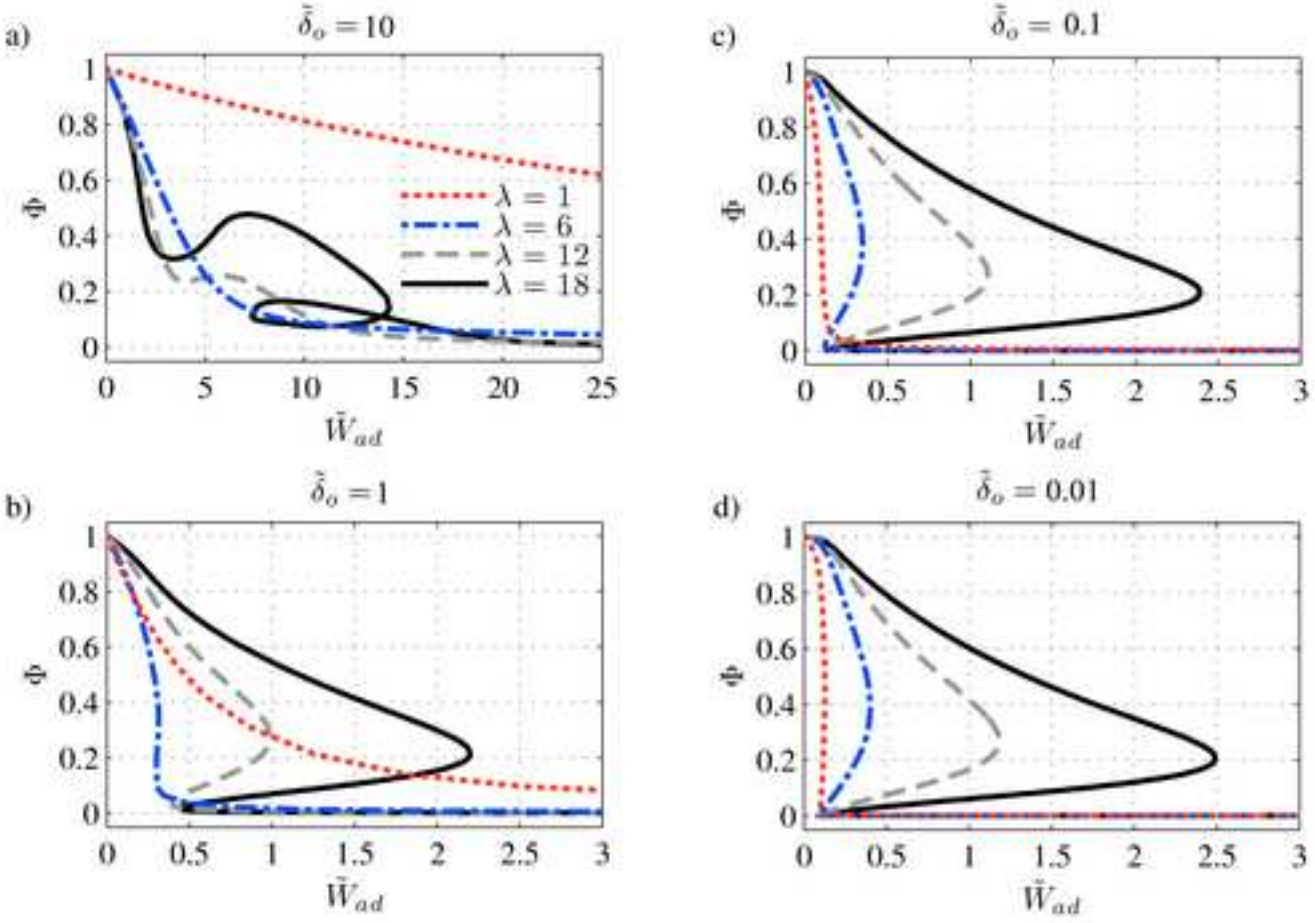

Figure(s)

Click here to download high resolution image

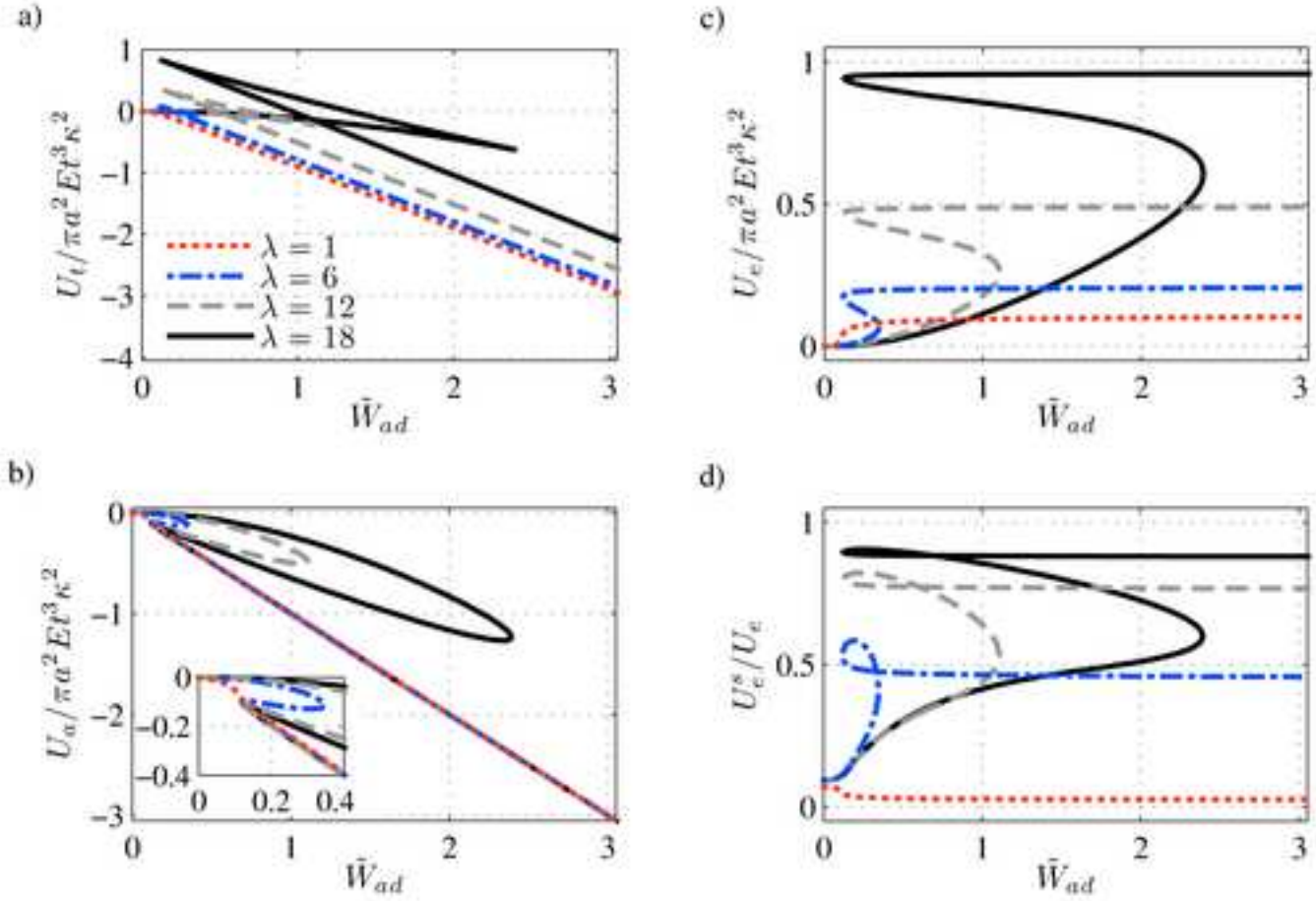

Figure(s)
Click here to download high resolution image

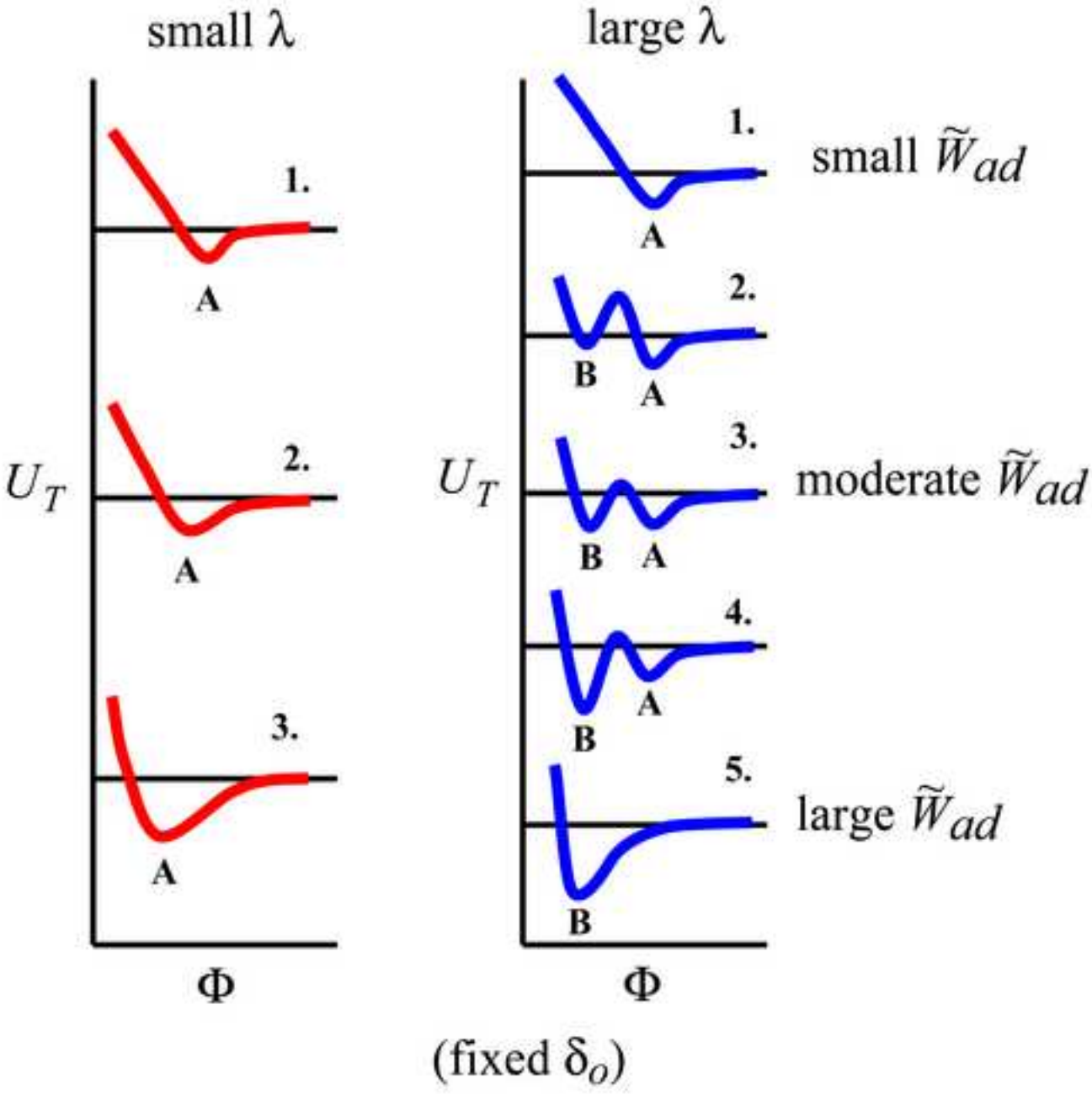

Figure(s)

Click here to download high resolution image

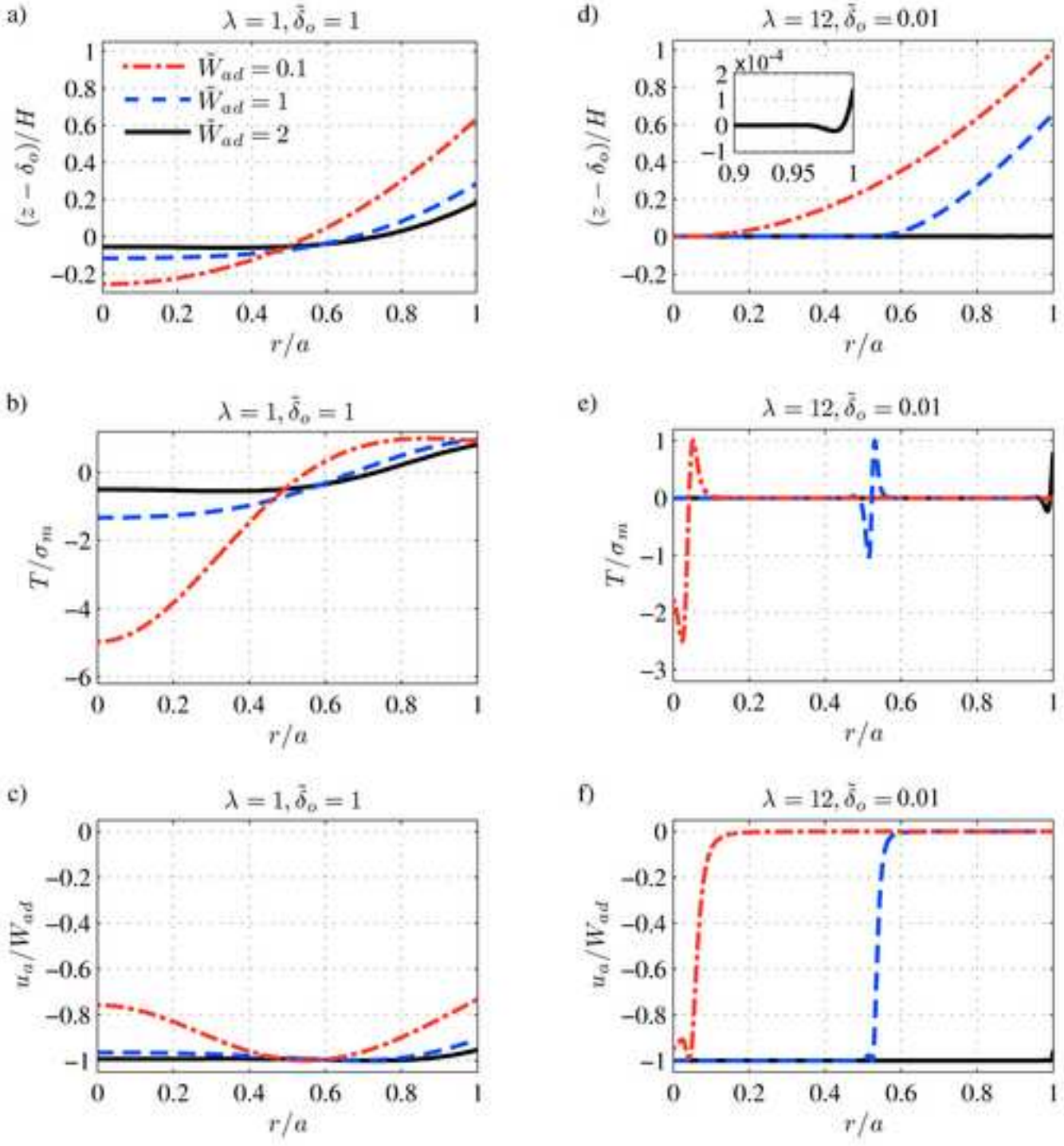

Figure(s)

Click here to download high resolution image

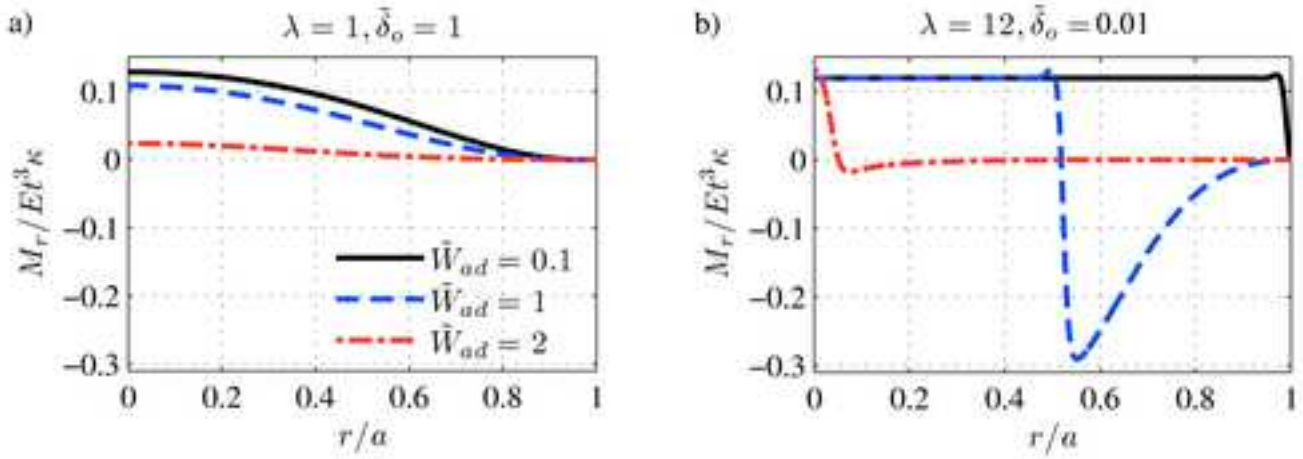

Figure(s)

Click here to download high resolution image

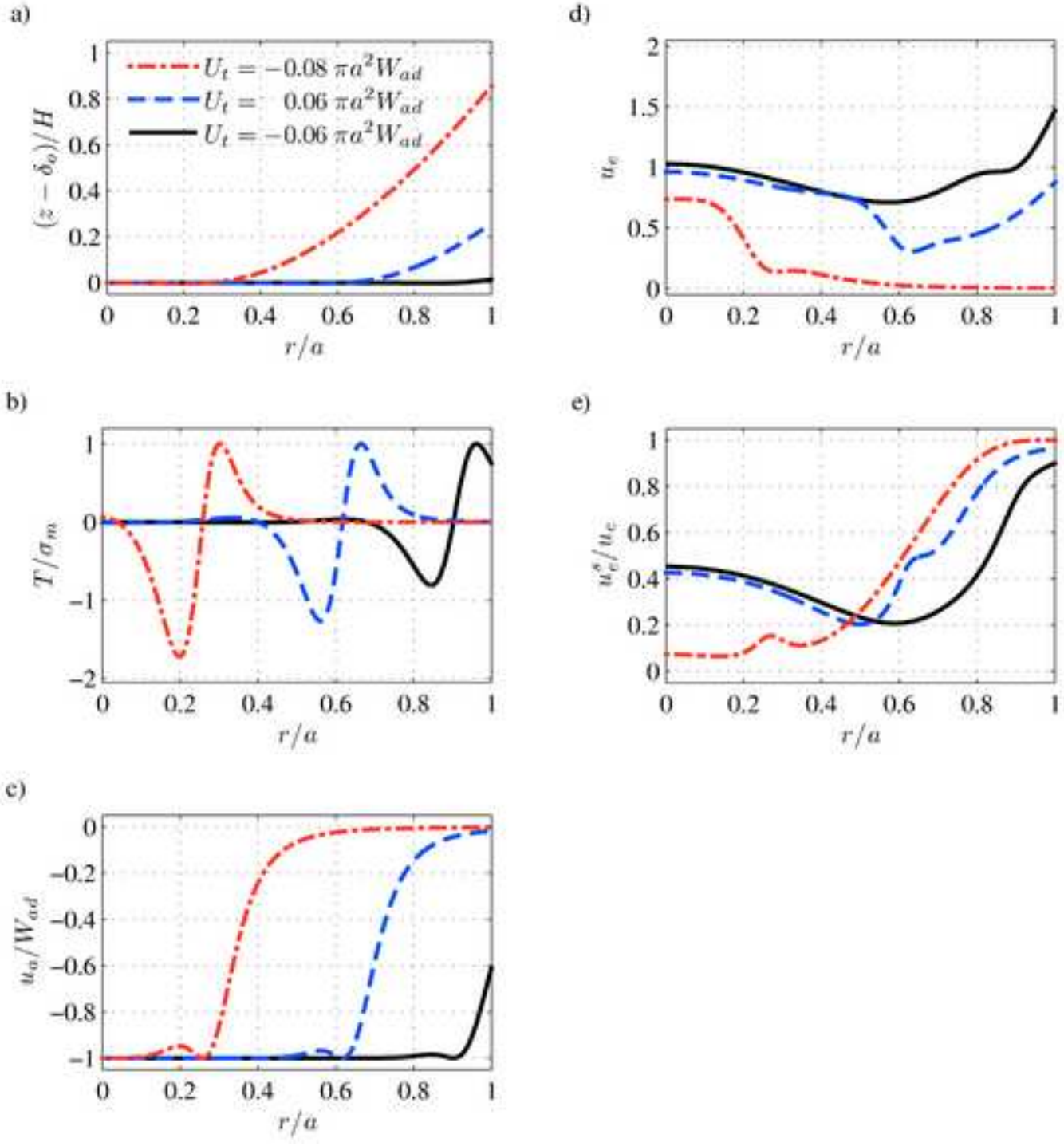

Figure(s)

Click here to download high resolution image

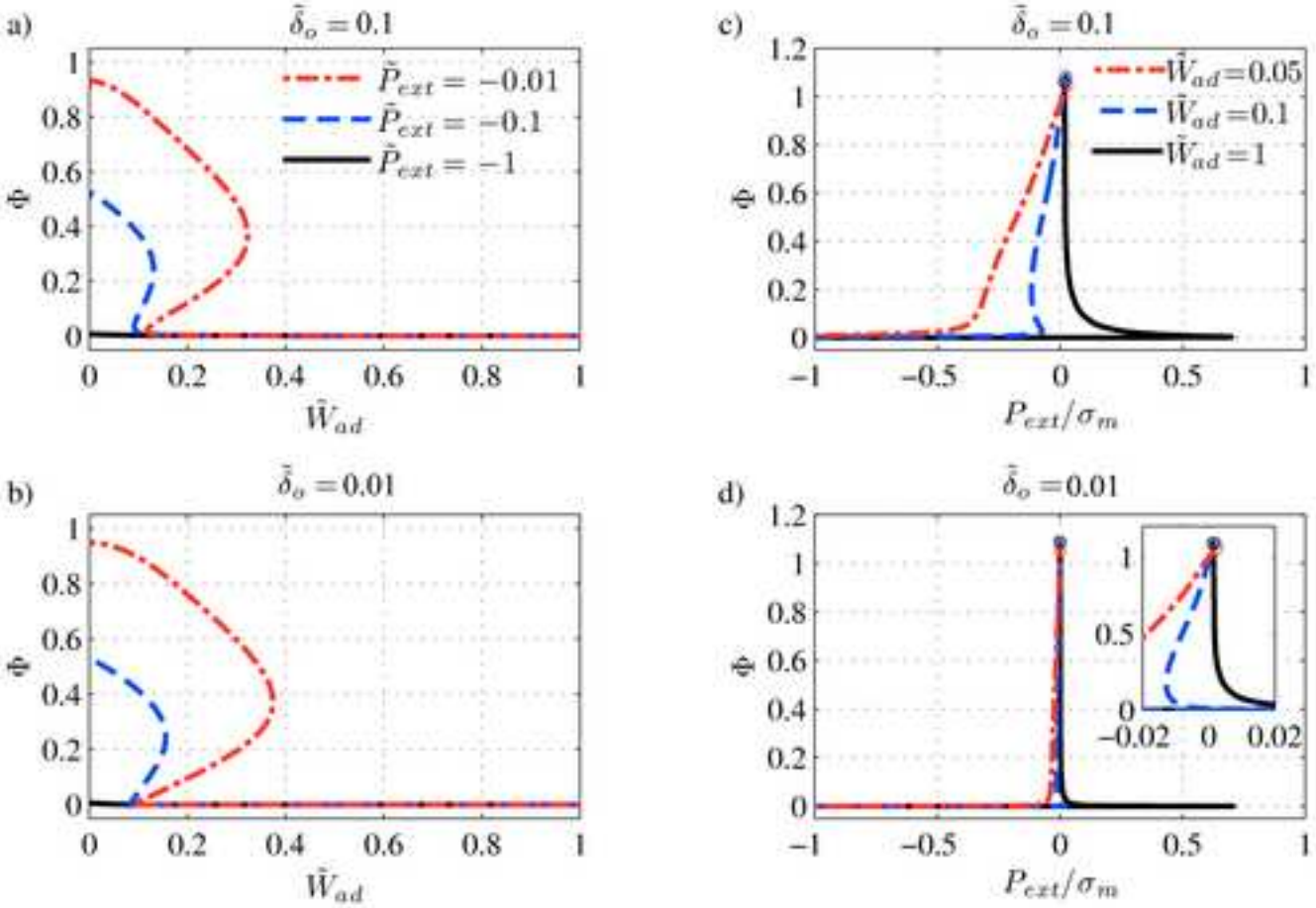

Figure(s)

Click here to download high resolution image

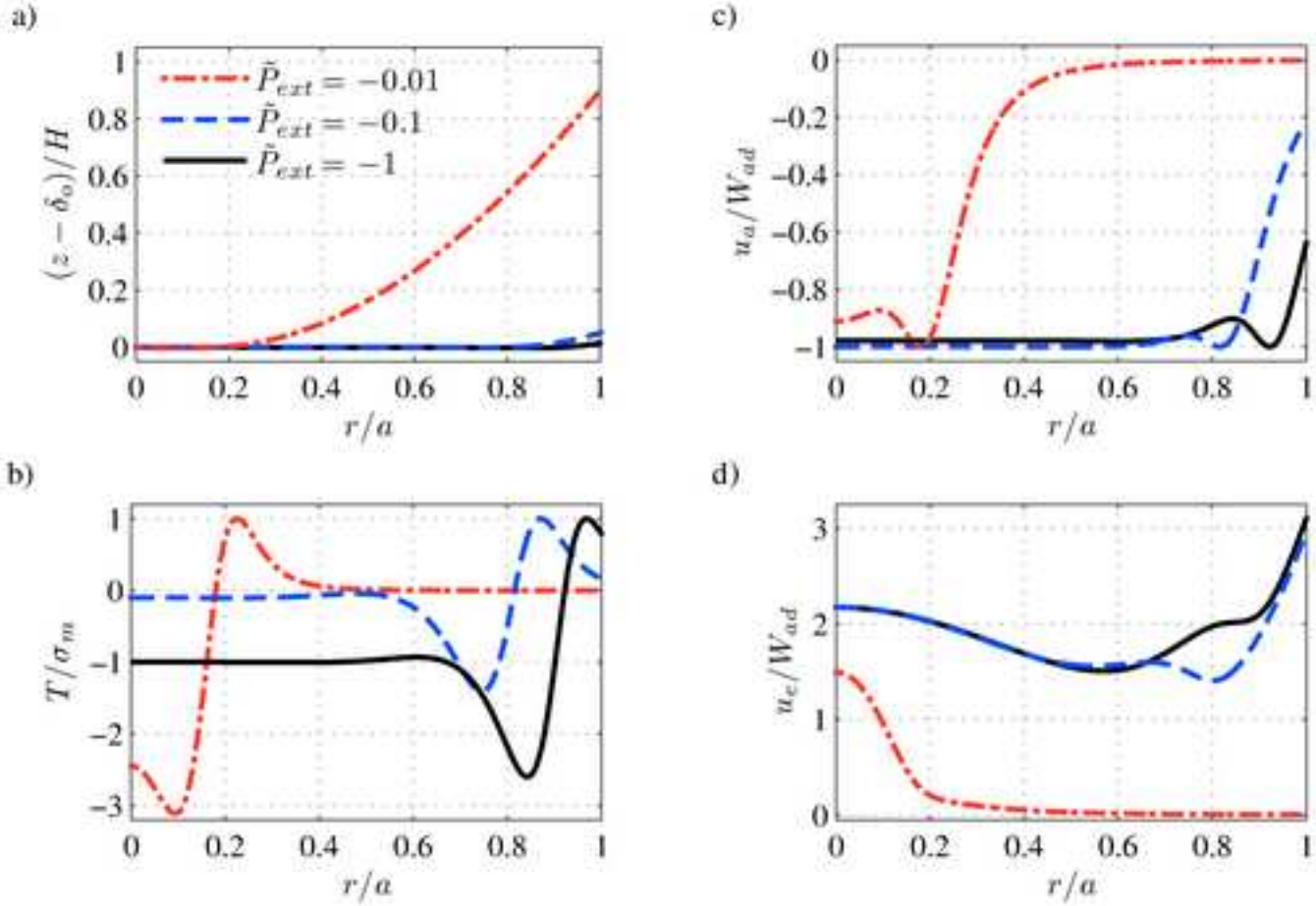

Figure(s)

Click here to download high resolution image

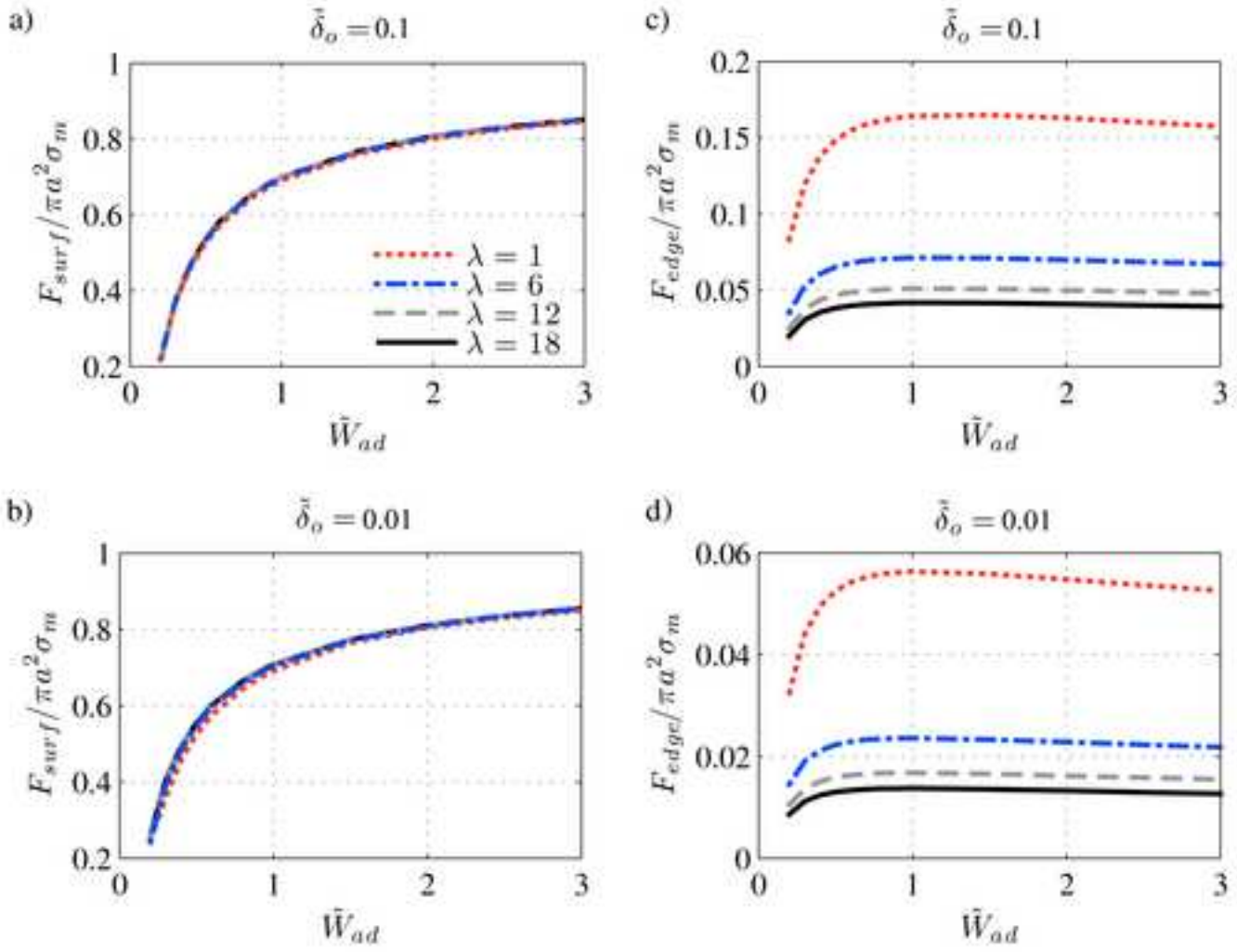

Table(s)

Click here to download high resolution image

	Wafer Bonding	Gold Nanocaps	Cell Adhesion	Lipid Bilayer
$E\left(\mathrm{N/m^2}\right)$	150×10^{9} [c]	69.1×10^{6} [e]	1×10^{3} [g]	8×10^{6} [k]
$t\,(\mathrm{m})$	1×10^{-3} [c]	12.5×10^{-9} [f]	0.4×10^{-6} [h]	4×10^{-9}
$a\,(\mathrm{m})$	50×10^{-3} [c]	55×10^{-9} [f]	10×10^{-6}	1×10^{-3}
$\kappa\left(\mathrm{m^{-1}}\right)$	3×10^{-2} [c]	20×10^{6} [f]	1×10^{5}	1×10^{3}
$H\,(\mathrm{m})$ [a]	38×10^{-6}	303×10^{-6}	10×10^{-6}	1×10^{-3}
$W_{ad}\left(\mathrm{J/m^2}\right)$	40×10^{-3} [c]	2 [d]	20×10^{-6} [i]	20×10^{-6} [i]
$\delta_o\,(\mathrm{m})$	0.15×10^{-9} [d]	0.18×10^{-9} [d]	15×10^{-9} [j]	10×10^{-9} [l]
$\sigma_m\left(\mathrm{N/m^2}\right)$ [b]	410×10^{6}	11.4×10^{9}	2.1×10^{3}	2.1×10^{3}
$\tilde{\delta}_o$	1×10^{-7}	1×10^{-2}	3.75×10^{-2}	2.5
λ	0.08	4.84	25	2.5×10^{5}
$\tilde{W}_{ad}$	0.30	0.04	31	1×10^{7}

Table(s)

Click here to download high resolution image

	$\tilde{\delta}_o = 1$	0.1	0.01	0.001
$\lambda = 1$	–/–	–/–	0.12/0.10	0.16/0.09
6	0.32/0.30	0.35/0.12	0.40/0.09	0.42/0.08
12	0.99/0.39	1.11/0.13	1.18/0.09	1.21/0.08
18	2.20/0.45	2.39/0.13	2.49/0.09	2.52/0.08

Table(s)

Click here to download high resolution image

	$\tilde{\delta}_o = 0.1$	0.01
$\tilde{P}_{ext} = -0.01$	0.32 / 0.12	0.37 / 0.09
-0.1	0.13 / 0.09	0.16 / 0.08
-1	$-/-$	$-/-$

Table(s)

Click here to download high resolution image

	$\tilde{\delta}_o = 0.1$	0.01
$\tilde{W}_{ad} = 0.05$	$-/-/0.028/-$	$-/-/0.002/-$
0.1	$-0.117/-0.073/0.025/-$	$-0.01/-/0.002/0.025$
1	$-/-/-/0.700$	$-/-/-/0.706$